Flow past a sphere: Predicting enhanced drag with shear-thinning fluids, dissipative and constant shear-viscosity models

I.E. Garduño[a,b], H.R. Tamaddon-Jahromi[a], M.F. Webster[a]*

[a]*Institute of Non-Newtonian Fluid Mechanics, Swansea University, College of Engineering, Bay Campus, Fabian Way Swansea, SA1 8EN, UK*

[b]*Centro de Ciencias Aplicadas y Desarrollo Tecnológico, Universidad Nacional Autónoma de México, C.U., Ciudad de México 04510, México*

Abstract

This article tackles the topic of drag detection for flow past a sphere, focusing on response for viscoelastic shear-thinning fluids, in contrast to constant shear-viscosity forms, both with and without extensional-viscous dissipative contributions. The work extends that previously of Garduño *et al.* [1], where experimental levels of resultant *drag-enhancement* were captured for Boger-fluids, using a new hybrid dissipative viscoelastic model. This advance was based on Finitely Extensible Non-linear Elastic and White-Metzner constructs, where the level of extensional-viscous material time-scale had to be considerably raised to provide strong strain-hardening properties. The new *dissipative model drag findings* are: - *for low-solvent* systems, all such models reflect only significant drag-reduction, with barely any distinction from base-level dissipative-factor response. Such systems consistently gave considerably more pronounced decline in *drag* than for their *high-solvent* counterparts. Alternatively, under *high-solvent systems (as in Boger fluids)*, the general observation for all four such dissipative models, is that after an *initial-decrease* in drag, *a second-increasing* trend can be extracted. This lies in stark contrast to base-level, null dissipative-factor drag findings, where *only drag-reduction* could be observed. Yet consistently, the inclusion of shear-thinning is reflected in the overall lowering of drag levels. Nevertheless, strong terminating drag-enhancement can be generated under larger dissipative-factor setting for *dissipative*-EPTT (shear-thinning, strain-hardening/softening), only slightly suppressed from that for *dissipative*-FENE-CR (constant shear-viscosity, strain-hardening/hardening-plateau). Other dissipative-{FENE-P, LPTT} variants, showed encouraging trends towards drag-enhancement, but unfortunately suffered from premature solution stunting, and hence, were restricted in accessible range of deformation-rates. In addition, an increase in geometry aspect-ratio, generally provokes elevation of drag, but only under high-solvent state, and hence only then, leads to evidence for stimulating drag-enhancement.

Keywords: Flow past a sphere, Boger fluid, shear-thinning fluid, dissipative time-scale, swanINNFM(q)-model

* Corresponding Author. *E-mail address:* m.f.webster@swansea.ac.uk

1. Introduction

This paper is a natural continuation to our earlier work in predicting flow past a sphere and capturing experimental levels of resultant *drag* for Boger fluids (see [1]). There, a new dissipative viscoelastic model was proposed, emerging from a combination of Finitely Extensible Non-linear Elastic (Chilcott and Rallison [2] and White and Metzner [3] models, termed swanINNFM(q). Constructively, such a model proved capable of generating considerable extensional viscosity response, and hence, counterpart *drag-enhancement*. In addition, variation of drag with respect to geometric aspect-ratio and solvent-fraction systems was also addressed, where both factors were found to influence and regulate drag-response. This new model has also been successfully trialed on other flow problems and deformation settings, such as on contraction-expansion flow and sharp-corner contraction flow, where experimental enhanced pressure-drops have been sharply captured ([4, 5]). Here, the major goal is to enter virgin territory, and pursue in contrast to constant viscosity fluids, the relative position on drag-response for fluids with varying levels of shear-thinning. The implication from general findings is that if drag-enhancement is to be gathered for larger Weissenberg number flows, the level of extensional-viscous material time-scale (dissipative base-factor parameter) must be considerably raised. In this respect, the fluid rheology plays a major role, and in particular, strong strain-hardening properties are crucially important.

The present research compares and contrasts drag response for a variety of fluid compositions and geometry-ratio flow specifications. A principal aim here has been to examine the impact of rheology on drag - through first, shear-thinning influence, and then extensional response, whilst incorporating strain-hardening to strain-softening properties. That is, taken alongside high-solvent and low-solvent fluid constitutions. The whole is accomplished by suitable model combinations, with and without additional dissipative components, selected from constant viscosity FENE-CR, to shear-thinning offerings, from FENE-P and PTT (Exponential and Linear). In addition, three geometry aspect ratios are considered to address increased severity in extensional deformation, covering a computational-benchmark base-case (aspect ratios of sphere:tube radii, $\beta_{sphere} = 0.5$, tightest-fit), and two others of $\beta_{sphere} = 0.4$ (medium-fit) and $\beta_{sphere} = 0.2$ (loosest-fit).

In this area, a significant contribution was made to the subject by Tamaddon-Jahromi *et al.* [6], in selectively including the effects of shear-thinning, through suitably chosen models from the class of Phan-Thien/Tanner (PTT) [7] models, with cross-reference to FENE-CR and Oldroyd-B models. There, the authors argued that the *drag-reduction* observed through Linear LPTT predictions, could be primarily attributed to the influence of shear-thinning (η_s).

One notes the literature coverage in Garduño *et al.* [1] on the constant shear-viscosity flow problem, and comparison therein, to the experimental Boger-fluid data of Jones *et al*. [8]. Consulting the literature more widely, a range of constitutive models have been employed in the prediction of drag, encountered as a consequence of flow past a sphere, of both analytical and computational form, whilst involving some depth of comparison to counterpart experimental findings; see for example, Walters and Tanner [9], Owens and Phillips [10], Tanner [11], and McKinley [12]. In an alternative set of experimental studies, Chen and Rothstein [13] measured the flow field around a sphere (aspect ratios of 0.0625 and 0.125) falling in a column of a wormlike micelle fluid-solution. For this purpose, the working fluid was characterized in both shear and transient homogeneous uniaxial extension. There, initially and at low deformation-rates, the fluid showed *drag-reduction* upon increasing Deborah number, which was attributed to *shear-thinning effects*. Yet, as the Deborah number was increased somewhat further, the establishment of a strong extensional flow in the wake of the sphere stimulated drag to increase, and to exceed that of an equivalent zero-shear-viscosity Newtonian fluid. Moreover, concerning the related problem of flow of Newtonian and non-Newtonian fluids around a circular cylinder, Coelho and Pinho [14] reported measurements of pressure on the cylinder surface. There, the non-Newtonian fluids were composed of aqueous solutions of CMC and tylose, that displayed varying degrees of shear-thinning and elasticity, at weight concentrations of 0.1–0.6%. Such experiments incorporated the transition to and with shear-layer transition regimes. These authors found that, for low Reynolds numbers flows, elasticity within the shear layers was responsible for an increase in drag reduction with rise in polymer concentration. Accordingly, the increase in wake-angle and pressure-rise coefficient for the more concentrated solutions, reduced the consequent drag-coefficient by narrowing the near-wake. For the case of the tylose solutions, good correlation was detected between the elasticity number and the mean pressure-rise coefficient. Furthermore, in the experimental work of Mendoza-Fuentes *et al*. [15], drag-correction factors were calculated for the creeping motion of spheres descending in various associative polymers. Different polymer concentrations were tested, for various sphere-container ratios and flow Weissenberg numbers. There, no increase in the drag-correction factor could be deduced, which was argued to be due to the simultaneous and opposing effects of extension-thickening and shear-thinning viscosity.

Furthermore, in experiments with a PAA/CS Boger fluid¸ Chhabra and Uhlherr [16] has found that for small values of $\beta_{sphere} = a/R < 0.3$ (ratio of sphere to tube radius), increasing fluid elasticity resulted in a reduction in the wall-drag and a rapid increase in the settling velocity at moderate Deborah number which asymptotically approached the value observed in the unbounded domain. In addition, in Arigo *et al.* [17], both experimental measurements and numerical predictions indicated that the wall correction factor for the motion of a sphere through a viscoelastic fluid is a sensitive function of the geometric

aspect-ratio and the Deborah number *(more than one ratio)*. These authors showed that non-Newtonian response, in the strong extensional flow near the rear stagnation-point, results in the formation of a pronounced viscoelastic wake (extending up to 30 sphere radii behind the sphere) and a downstream shift in the streamlines. The measurements of the drag correction factor for $\beta_{sphere} = a/R < 0.25$ confirm the trends observed in earlier measurements with PIB/PB Boger fluids of Jones *et al*. [8] and Becker *et al.* [18]. Their measurements of the wall correction factor and fluid velocity field at high $a/R < 0.4$ also corroborated the conjecture of Jones *et al*. [8] - that the wall correction factor apparently decreases below the Newtonian value. It was argued that this was due to the rapid non-linear reduction in the settling velocity at high *a/R,* and the resultant lowering of the effective strain-rates, near the rear stagnation-point and in the downstream wake of the sphere.

Concerning other major findings on Boger fluids, Rasmussen and Hassager [19] used a Lagrangian finite element method and a Rivlin-Sawyers constitutive equation, to simulate the transient sedimentation of spheres in polymeric liquids. Calibrated against experiments with a PIB/C14/PB test-fluid (of Becker *et al.* [18]), computational solutions over-predicted observed drag, noting about 21% drag increase at a Deborah number of 4.55, on account of the elongational flow in the wake region. Jin *et al.* [20] presented an extended EEME/SUPG formulation covering UCM and the PTT steady solutions in the absence of solvent viscosity. Findings for the UCM model agreed well with those of Lunsmann *et al.* [21], up to a Weissenberg number 2. Solution reported for the PTT model, up to a Weissenberg number of about 4.5 displayed only drag-reduction, argued as due to shear-thinning response. Song *et al.* [22] used commercial software (COMSOL) to solve the same flow problem for four constitutive models (Newtonian, Carreau, Oldroyd-B and PTT), establishing good agreement between their calculations and the literature. Incorporation of either shear-thinning or elasticity led to a decrease in drag-coefficient. Moreover, a velocity-overshoot was observed in the wake on the flow-centreline, resulting from interaction between contributions from shear-thinning and elasticity. Zheng *et al.* [23, 24] used a boundary element method to examine the influences of inertia (Reynolds numbers from 0 to 150), shear-thinning and fluid-elasticity (with a PTT model), contrasting predictions against those for inertial Newtonian fluids and inelastic non-Newtonian fluids. Relatively speaking, shear-thinning and elasticity led to drag-reduction, whilst inertia (Reynolds number rise) promoted drag-enhancement.

Abedijaberi and Khomami [25] employed multiscale flow simulation for a highly-elastic dilute polymeric solution. Through comparisons with Boger Fluid steady-state experimental measurements (of solvent fraction 0.59), they demonstrated the predicted growth-evolution of drag coefficient as a function of fluid elasticity (for various models, multiscale and single-scale). The experimental data was accurately predicted at high *Wi (beyond 4),* when using realistic multi-segment micromechanical

models; noting the early dip for *Wi*<1 and subsequent rise to enhanced levels for *Wi*>2. Notably, macromolecular dynamics is described under such micromechanical models, whilst also the transient extensional viscosity of the experimental fluid is closely captured (theoretically) at high extension rates. Some shear-thinning predictions with FENE-P were also provided, but these indicated only *modest rise* in drag coefficient beyond their *Wi*~1, approaching the unity drag coefficient reference line, whilst plateauing by *Wi*~6.

A recent contribution to this topic on shear-thinning/viscoelastic fluids is by Housiadas and Tanner [26]. Their analytical work consists of high-order perturbation solutions for steady sedimentation of a sphere in a viscoelastic fluid. Key conclusions drawn from that work lie in agreement with present findings in that: after an initial decrease in drag force, predicted at small Deborah numbers (*De*), subsequently there is significant drag enhancement, at larger Deborah numbers. Nevertheless, for *large De*>0.8, and values of ε_{PTT} >0.3 (ε_{PTT} , PTT rheological parameter), these analytic perturbation solutions were found to predict negative wakes around the equator (which were taken as analytically invalid, according to their positive definiteness criteria supplied in [26]). Our experience on this issue is that, when a full-solution evolution is attempted, as in López-Aguilar *et al*. [27, 28], such a *localised* loss of positive definiteness may arise consistently within complex inhomogeneous flow. This may be stimulated by a flow singularity, for example as here, without destroying the global steady-state solution. Indeed, this is necessary to support intermediate *Wi*-solution development through steady-states, see López-Aguilar *et al*. [27, 28].

2. Governing equations and flow problem

Under incompressible isothermal conditions, the behaviour of viscoelastic flow is governed by the fundamental principles of conservation of mass and momentum. In non-dimensional form, these are respectively given as:

$$\nabla\cdot\boldsymbol{u}=0 \tag{1}$$

$$Re\frac{\partial\boldsymbol{u}}{\partial t}=\nabla\cdot\boldsymbol{T}-Re\,\boldsymbol{u}\cdot\nabla\boldsymbol{u}-\nabla p\,. \tag{2}$$

Here, a spatial-temporal bounded domain is considered, with $\boldsymbol{x}$ and t taken as the associated spatial and time coordinates; field variables $\boldsymbol{u}, p$ and $\boldsymbol{T}$ represent fluid velocity, hydrodynamic pressure and stress tensor expressed as:

$$\boldsymbol{T}=\boldsymbol{\tau}_p+\boldsymbol{\tau}_s=\boldsymbol{\tau}_p+2\beta_{\text{solvent}}\boldsymbol{d}. \tag{3}$$

The stress tensor decomposes into two parts, a polymeric extra-stress contribution ($\boldsymbol{\tau_p}$) and a Newtonian stress contribution ($\boldsymbol{\tau_s}$). Here, $\boldsymbol{d} = \left(\nabla \boldsymbol{u} + \nabla \boldsymbol{u}^{\dagger}\right)/2$ represents the rate of deformation tensor, where superscript † denotes tensor transpose. In addition, the non-dimensional group number of Reynolds number may be defined as $Re = \left(\rho U_{char} L_{char} / \mu_0\right)$, with characteristic scales of U_{char} on fluid velocity (terminal velocity of the sphere), and $L_{char} = a$ (sphere radius) on spatial dimension. In addition, ρ represents the material density and reference viscosity $(\mu_\circ)$ is characteristic viscosity taken as a zero shear-rate viscosity ($\mu_0 = \mu_p + \mu_s$). Here, μ_p is a polymeric viscosity and μ_s is a solvent viscosity component, so that a solvent-fraction can be expressed as ($\beta_{\text{solvent}} = \mu_s / \mu_0$).

2.1 Constitutive modelling: FENE-CR, FENE-P, PTT, FENE/PTT, swanINNFM(q) [sIq] models

Chilcott and Rallison [2], and Phan-Thien and Tanner [7] constitutive models can be solved in two forms, either stress tensor or configuration tensor form. In our earlier study (Tamaddon-Jahromi *et al.* [6], the LPTT fluids utilised the stress tensor form and critical stress states achieved were for much lower elasticity levels ($Wi \leq 4.5$, see below for definition). As a consequence, the current work utilises a configuration tensor form of the PTT and FENE-CR models, in contrast to the specific stress tensor form. Moreover, one seeks a constitutive model that leads to a constant shear viscosity (FENE-CR) and the influence of shear-thinning (hence advent of PTT) in the context of strain-hardening/softening properties. Strain-softening is introduced via EPTT solutions in contrast to strain-hardening properties of LPTT and FENE-CR. Following Garduño *et al.* [1], Tamaddon-Jahromi *et al*. [4, 29], and López-Aguilar *et al*. [5], and the constitutive equation for the FENE-CR and PTT models (see associated rheometrical functions in Figure 1) provide the following expression through a conformation transformation and a configuration tensor **A**, as:

$$Wi\, \overset{\nabla}{\mathbf{A}} + f(Tr(\mathbf{A}))(\mathbf{A} - \mathbf{I}) = 0. \tag{4}$$

Here, $\overset{\nabla}{\mathbf{A}}$ is the upper-convected material derivative of stress (**A**), defined by

$$\overset{\nabla}{\mathbf{A}} = \frac{\partial \mathbf{A}}{\partial t} + \mathbf{u} \cdot \nabla \mathbf{A} - (\nabla \mathbf{u})^{\dagger} \cdot \mathbf{A} + \mathbf{A} \cdot (\nabla \mathbf{u}). \tag{5}$$

The corresponding $f(Tr(\mathbf{A}))$ for the FENE-CR, FENE-P (Chilcott and Rallison [2], and PTT (Phan-Thien and Tanner [7]) are given by:

$$f(Tr(\mathbf{A})) = \frac{1}{1 - Tr(|\mathbf{A}|)/L^2_{FENE}} \qquad \text{FENE-CR, FENE-P} \tag{6}$$

$$f(Tr(\mathbf{A})) = 1 + \varepsilon_{LPTT} Tr\left(|\mathbf{A} - 3|\right) \quad \text{LPTT,} \tag{7}$$

and $$f(Tr(\mathbf{A})) = exp\left(\varepsilon_{EPTT} Tr\left(|\mathbf{A} - 3|\right)\right) \quad \text{for EPTT.} \tag{8}$$

Above, **I** is the identity tensor, L_{FENE} is extensibility parameter for FENE-CR model, and ε_{PTT} is the constant parameter for PTT model, which governs the non-linear function $f(Tr(\mathbf{A}))$. Both parameters mainly dictate severity in strain-hardening.

One notes that, for the FENE-P model eq. (4) is amended to:

$$Wi \overset{\nabla}{\mathbf{A}} + \left[f(Tr(\mathbf{A}))\mathbf{A} - \mathbf{I} \right] = 0. \tag{9}$$

Then, typically, the following Kramers' expressions relate stress and configuration tensors Garduño *et al.* [11]:

$$\boldsymbol{\tau} = \begin{cases} \dfrac{(1-\beta_{\text{solvent}})}{Wi} f(\text{Tr}(\mathbf{A})(\mathbf{A} - \mathbf{I}) & \text{for FENE - CR} \\ \dfrac{(1-\beta_{\text{solvent}})}{Wi} (f(\text{Tr}(\mathbf{A})\mathbf{A} - \mathbf{I}) & \text{for FENE - P} \end{cases}. \tag{10}$$

Furthermore, following [1, 4, 5, 29], a combination of FENE-CR and PTT models with the extensional White-Metzner model, has also been investigated (see related rheometrical functions in Figure 1). The new resulting class of swanINNFM(q) models may be expressed as:

$$\boldsymbol{T} = \boldsymbol{\tau}_p + \boldsymbol{\tau}_s,$$
$$\boldsymbol{\tau}_p = \frac{(1-\beta_{\text{solvent}})}{Wi} \text{f}(\text{Tr}(\mathbf{A}))(\mathbf{A} - \mathbf{I})\phi(\dot{\varepsilon}),$$
$$\boldsymbol{\tau}_s = 2\beta_{\text{solvent}}\phi(\dot{\varepsilon})\boldsymbol{d}, \tag{11}$$

Where $\dot{\varepsilon}$ is the invariant extensional strain rate defined as $\dot{\varepsilon} = 3\mathbf{III}_d / \mathbf{II}_d$, with second ($\mathbf{II}_d$) and third ($\mathbf{III}_d$) invariants of the rate-of-deformation tensor taken as,

$$\boldsymbol{II}_d = \frac{1}{2}\text{tr}\left(\boldsymbol{d}^2\right), \quad \boldsymbol{III}_d = det\left(\boldsymbol{d}\right). \tag{12}$$

Here, $\phi(\dot{\varepsilon})$ is taken as a quadratic truncated-approximation of the full cosh-exponential form, defined as $\phi(\dot{\varepsilon}) = 1 + (\lambda_D \dot{\varepsilon})^2$, with a dissipative material time-scale parameter of (λ_D) as in [1]; see [4] for alternative dissipative function forms.

The swanINNFM(q) model was originally developed to tackle various key unsolved benchmark viscoelastic flow problems, via a continuum-based differential formalisation, whilst seeking validation against existing well-founded experimental evidence. The benefits and advantages of this proposed new swanINNFM(q) model are: it displays the desired rheometric properties of: constant shear viscosity, finite extensibility (with a bounded extensional viscosity reaching an ultimate plateau), and a first-normal stress-difference weaker than quadratic. It has already proven well capable of capturing the elevated levels of some experimental data constituting enhanced pressure drops in contraction flows [4, 5] and drags in settling flows [1]; to date, this has not proven possible with any other *continuum-based* model. The model is derived from two highly reputable rheological models (FENE, White-Metzner). By necessity, an additional rheometric parameter, (λ_D), is required, which may be derived from extensional rheometry.

The non-dimensional group Weissenberg number is defined as $Wi = \lambda_1 U_{char} / L$, with dependency upon a single relaxation time (λ_1), U_{char} is a characteristic velocity (terminal velocity of sphere, U) and L is a characteristic length-scale (generally interpreted as the radius of sphere). In this form, one might increment the Weissenberg number (*Wi*) in numerical computations, by raising U/a at fixed fluid relaxation time, λ_1.

In addition, taking $\beta_{\text{sphere}} = 0.5$ as a base-instance of geometry and whilst adjusting geometric aspect-ratio through the length-scale (sphere-radius, or equivalently, of tube), one may obtain a functional relationship between the Weissenberg numbers for the three independent geometric aspect-ratios employed, to derive a common reference and basis for interpretation. So that with,

$$Wi_{\beta_{\text{sphere}}=0.5} = \lambda_1 \, \mathrm{U}/a_{\beta_{\text{sphere}}=0.5},$$

$$Wi_{\beta_{\text{sphere}}=0.4} = \lambda_1 \, \mathrm{U}/a_{\beta_{\text{sphere}}=0.4}, \qquad (13)$$

$$Wi_{\beta_{\text{sphere}}=0.2} = \lambda_1 \, \mathrm{U}/a_{\beta_{\text{sphere}}=0.2}.$$

Then, it follows that:

$$\frac{Wi_{\beta_{\text{sphere}}=0.5}}{Wi_{\beta_{\text{sphere}}=0.4}} = \frac{\mathrm{U}/a_{\beta_{\text{sphere}}=0.5}}{\mathrm{U}/a_{\beta_{\text{sphere}}=0.4}} = \frac{1}{0.8} = 1.25,$$

$$\frac{Wi_{\beta_{\text{sphere}}=0.5}}{Wi_{\beta_{\text{sphere}}=0.2}} = \frac{\mathrm{U}/a_{\beta_{\text{sphere}}=0.5}}{\mathrm{U}/a_{\beta_{\text{sphere}}=0.2}} = \frac{1}{0.4} = 2.5. \qquad (14)$$

2.2 Material functions: PTT/FENE-swanINNFM(q) models

The rheometrical response for the base-models, LPTT, EPTT, FENE-CR, FENE-P, and new models, FENE/PTT swanINNFM(q), are displayed in Figures 1 and 2. The particular model parameters selected for consideration are those covering high and low solvent-fraction fluids, $\beta_{\text{solvent}}=\{0.9,\ 1/9\}$, and those for dissipative factor $\lambda_D=\{0.0,\ 0.1,\ 0.2\}$. Here, the present study isolates and resolves rheological differences, where the parameters selected are used to draw out the individual influences of shear-thinning, strain-hardening, strain-softening and strength of solvent-fraction, respectively. This is accomplished by appealing to comparative results for FENE-CR (constant shear-viscosity), FENE-P and PTT (shear-thinning viscosity) models (see Figure 1a). In this respect, matching extensional viscosity response has been configured, for both FENE-CR(L=5) and FENE-P(L=5) models, against that for the PTT models, at a parameter value of ε_{PTT}=0.042 (moderate-hardening scenario). The FENE-P response is employed as somewhat of a *'tracker'* of LPTT response, under viscometric flows.

Initially, solutions for EPTT and LPTT models were generated with β_{solvent}=0.9 (90%, Figure 1a), at a peak plateau-level of extensional viscosity characterized by $(\varepsilon_{PTT}=0.042)$. In terms of shear viscosity, the LPTT (and FENE-P) fluid possesses almost the same characteristics as an EPTT fluid (same parameters), with the exception that EPTT response thins a little faster than with LPTT; the key distinguishing feature lies in their respective extensional viscosities. Then, the switch of solvent-fraction to β_{solvent}=1/9 (~10%, Figure 1b), reduces the second-plateau of shear-viscosity to relatively low-levels, thus stimulating a considerable increase in the rate of shear-thinning. In addition with change of solvent-fraction, there is a reduction in the second-plateau of EPTT extensional viscosity, which exaggerates the rate and degree of strain-softening. Note that under LPTT solutions, any strain-softening characteristics are suppressed, so that extensional viscosity level increases up to a terminating plateau at high extension-rates, where the level depends on the ε_{PTT} –parameter selected. This level is itself amplified by one decade with switch of solvent-fraction to β_{solvent}=1/9.

Typical rheometric behaviour is also matched in first normal stress-difference (see Figure 1b). Here, noted differences arise in N_1 at rates above {$5\text{x}10^0$ units, β_{solvent}=0.9} and {10^1 units, β_{solvent}=1/9}, when comparing the four base-models of EPTT, LPTT, FENE-P and FENE-CR. Above these rates, significantly larger N_1-values (by one decade) are observed at higher rates under the highly-polymeric state of β_{solvent}=1/9, when compared against that for β_{solvent}=0.9. The peaks and limiting high-rate N_1-

values vary, and are weakest for EPTT, less than LPTT, which itself is weaker than FENE-CR. Note that, almost identical N_1-values are observed between LPTT and FENE-P models.

Furthermore for the new proposed models, only extensional viscosity response is affected. This is shown in Figure 2, comparatively between values of λ_D=0.1 and λ_D=0.2, and also with cross-reference to base-response with λ_D=0.0 at each individual level of λ_D. This also implies that for any given fluid and its rheometric data, that the λ_D-parameter may be determined by fitting to the extensional viscosity. Again, both solvent-fraction data are represented, that display up-scaling by one order from β_{solvent}=0.9 to β_{solvent}=1/9, following trends as above. Here, an increasing trend in η_e is clearly apparent for new swanINNFM(q) forms, when compared to their base-forms, FENE-CR and PTT. Focusing on the more exaggerated comparison between λ_D=0.2 and λ_D=0.0 data, one observes departure from η_e-plateau limiting-form to ultimate strain-hardening, at rates of {10^1 units, β_{solvent}=1/9} and {10^0 units, β_{solvent}=0.9} with FENE and LPTT variants. At comparable rates, the switch in EPTT-response is from strain-softening to strain-hardening; hence, more striking. Then, with elevation of dissipative factor from λ_D=0.1 to λ_D=0.2, essentially only the hardening-level is raised, to ultimately about half a decade. For larger values of $\lambda_D = 0.5$ and $\lambda_D = 1.5$, one may refer to Garduño *et al.* [1] for more detail on material response under swanINNFM(q) with FENE-CR.

3. Problem specification and numerical approximation

In this work, three different geometric-problems are selected for study, with sphere-to-tube wall radii aspect-ratios of $\beta_{\text{sphere}} = \{0.5,\ 0.4,\ 0.2\}$. Here, sphere radius (size/mass) is considered as constant and tube-radius is the actual length-scale adjusted, to provide the relevant aspect-ratios. Corresponding schematic diagrams for the various geometric configurations are provided in Figure 3a. The $\beta_{\text{sphere}} = 0.5$ meshing used reflects 2687 quadratic elements and 5610 nodes with 35122 degrees of freedom. One may refer to Garduño *et al.* [1] for further detail on meshing for the falling sphere problem, which provides a mesh refinement analysis for some typical base-case studies (see Figure 3b, Table 1); and below, under the refined mesh solutions of Figure 5. In addition, two values of $\beta_{\text{sphere}} = 0.9$ and $\beta_{\text{sphere}} = 1/9$ are also considered. Steady creeping flow is assumed ($Re \approx 10^{-2}$) and as a result, the momentum convection term contribution is negligible. The flow is assumed to be axisymmetric and the frame of reference is moving with the sphere. Hence, for ease of computational implementation, the tube wall is assumed to move past the sphere at a constant velocity. In this work,

the dimensionless drag force on the sphere is evaluated by integrating the pressure and stress components over the sphere surface that may be represented as:

$$D = 2\pi R_s^2 \int_0^{\pi} \left\{ T_{rz} \sin(\theta) + (T_{zz} - p)\cos(\theta) \right\} \sin(\theta)\, d\theta \qquad (15)$$

The so-called Stokes drag force on a sphere falling in an unbounded Newtonian fluid is given by $D_\infty = 6\pi\mu R_s U_\infty$. Here, $R_s = a$ is the sphere radius, whilst μ is the viscosity of the fluid and U_∞ is the fluid velocity far from the sphere. The *drag coefficient* is then defined through $K = D/D_\infty$. Note that, the *drag correction factor* (K/K_N) shown in the results section is due to adjustment in base K_N-values (Newtonian-drag).

3.1 Numerical discretisation

Hybrid finite element/finite volume scheme: The numerical technique employs a hybrid combination of *semi-implicit Taylor-Galerkin/incremental pressure-correction algorithm*, to discretise and solve the momentum-continuity governing equations, with a *cell-vertex finite volume sub-cell technique* for stress. The base finite element technique has appeared previously in Carew *et al*. [30] in its various stages of derivation; the novel algorithmic aspects here centre around the finite volume stress approximation. Herein, only a brief description of the procedure and steps is presented. The scheme incorporates a *time-stepping procedure* and a *fractional-staged equation* methodology over each time-step. The fractional equation procedure is represented in some three phases: first, a mass-matrix form; second, a Poisson-equation type; and third, a corrected mass-matrix form. The numerical solvers include a Jacobi iteration method for the first, third stage, performing three mass-matrix iterations per step, and a direct Choleski decomposition method at stage two. For a reasonable balance between accuracy and stability, a time-step of 10^{-4} is adopted throughout all calculations. The velocity field introduces a finite-element piecewise continuous approximation based on quadratic shape functions, and the pressure field is approximated similarly by linear shape functions.

Sub-cell finite volume stress discretisation: For the configuration stress-variable tensor, a *triangular-subcell cell-vertex finite volume* approach is developed (Wapperom and Webster [31]; Aboubacar and Webster [32]; Webster *et al*. [33]; Belblidia *et al.* [34, 35]), where a parent-triangular finite-element is sub-divided into four finite-volume subcells (child-triangles). The individual components of the configuration stress-variable tensor are then approximated by linear shape functions over each subtended triangular finite-volume (*fv*) child-subcell. This is accomplished via integral flux and source term evaluation over each finite volume triangular sub-cell. Contributions over the full *fv*-child-subcell, are then allocated proportionally by the selected cell-vertex distribution scheme (*LDB-method*

upwinding) to the three vertices of that *fv*-child-subcell. Likewise, contributions on the *subtended* median-dual-cell (*MDC*) zone of the *fv*-child-subcell are also allocated to the designated *MDC*-node of that subcell. In this manner, nodal configuration-variable values (A_l) are computed at the vertices (l) of each *fv*-child-subcell (cell-vertex oriented form).

The corresponding configuration-variable nodal update is then derived by summing all contributions from its control volume, which is composed of all *fv*-triangles surrounding a particular node. This is illustrated through the generalised time-accurate nodal-update stencil for configuration-variable (*CT3*-scheme of Aboubacar and Webster [32]), which has become a standard basis for such schemes. Such a form incorporates both flux and source terms (split), with appropriate area-weighting between fluctuation-distribution and *MDC*-contributions. Fluctuation-distribution upwinding factors are themselves denoted through the α_l^T -dependency.

Further to the above, two additional and most recent strategies are introduced, as discussed at length elsewhere in López-Aguilar *et al*. [27, 28] under the context of thixotropic modelling - that is ***ABS-f-correction and VGR-correction***. The former avoids the possibility of the dissipation function becomes negative, thus predicting negative values of the f-functional during flow evolution. The latter refers to the particular velocity-gradient recovery-correction procedure (VGR-correction), imposed solely on the centreline, which prevents build up of spurious numerical noise in solution evolution. Note that, at the first non-zero *Wi*-solution stage, simulations commence from a quiescent initial state for all variables. Subsequently, continuation in Weissenberg number is employed (through increase of sphere velocity). The inlet boundary condition (shear-flow) for the conformation tensor **A** are taken to be $A_{11} = 1 + \left(Wi^2 * \dot{\gamma}^2\right) / f^2$, $A_{22} = A_{33} = 1$, and $A_{12} = 1 + \left(Wi * \dot{\gamma}\right) / f$, where $\dot{\gamma}$ is the shear rate. This differentiates between the various models in pure shear flow. In addition, use of the configuration tensor generally ensures that positive definiteness is satisfied within the solution evolution (see [27]).

4. Drag Results for individual geometries: Fixed geometry $\beta_{\text{sphere}} = 0.5$

4.1 ***Drag for four base models:*** FENE-CR, FENE-P (L=5), LPTT, EPTT (ε_{PTT} =0.042), (β_{solvent} =0.9, 1/9), λ_D =0.0 (Figure 4)

First, a comparison is conducted on drag results, across model options with rheological variations, within the context of a single fixed geometry-ratio, that of the base-reference of $\beta_{\text{sphere}} = 0.5$, a computational benchmark. This offers direct back-reference, between shear-thinning response and that derived earlier with constant-viscosity approximations (*FENE-CR*). Figure 4 provides such data on *drag correction factor* against increasing Weissenberg number (*Wi*). Here, two levels of solvent

fraction are considered, grouped as shown, β_{solvent}=0.9 (high-solvent, low-solute) and $\beta_{\text{solvent}}=1/9$ (low-solvent, high-solute), whilst contrasting the variety of response due to rheological variation over the four-base constitutive models, (FENE-CR, FENE-P, LPTT, and EPTT) (λ_D=0.0).

High-solvent* (β_{solvent}=0.9) *findings: Here, all models display an initial declining trend in drag, which persists up to *Wi*=6.0. Quantitatively, the *drag correction factor* has dropped to around ~3% below the Newtonian reference line with constant-viscosity FENE-CR; under shear-thinning counterparts (FENE-P and PTT), the associated drop doubles to ~7%, a common finding and experience reported in general. On drag variation over $0.1 \leq Wi \leq 4$, between LPTT and FENE-P, with matching peak-plateaux in extensional viscosity response - here, FENE-P supports lower *drag*-values than does LPTT, attributable to the lower degree of hardening (and slightly lower η_s) for FENE-P at low-rates (see Figure 1, zoomed sections). Note that, both models show almost an identical shear viscosity (η_s) beyond rates ~10^0, and first normal stress difference (N_1) uniformly. Furthermore, the FENE-P drag-results overlap with those for the EPTT fluid for *high-solvent* (β_{solvent}=0.9) fluids. This would indicate that high-solvent options do not enter deformation-rate regimes of rheological distinction, in contrast to their *low-solvent* counterparts (see below) One notes the (η_e, N_1) zones of influential dominance between these two models [6].

Low-solvent* (β_{solvent}=1/9) *findings: With the switch from high-to-low solvent content (same $\beta_{\text{sphere}}=0.5$), there is a major impact on overall drag-level, reflected in Figure 4. As anticipated, *high-solute* (β_{solvent}=1/9) solutions show considerably more pronounced decline in *drag* than for their *high-solvent* counterparts. This is due to the relative proportions of solvent-to-polymeric components within each fluid-system. Amongst this data, the FENE-CR drag (Boger fluid) proves to be the least suppressed, and is found to reach to its limiting solution-level of *Wi* (~Wi_{crit}=2.5), somewhat earlier than for shear-thinning alternatives. In addition, the exponential PTT (EPTT) model, with *strain-hardening/softening* properties, provides a considerably wider solution-range of elasticity (up to *Wi*=6); noticeably so, when compared to its linear counterpart LPTT (Wi_{crit}=3.5), that displays substantial *strain-hardening* response. Moreover, *drag* results reveal only modest departure between both forms of PTT at the same *Wi*-levels, with slightly deeper decline in EPTT-drag (attributable to its slightly more exaggerated shear-thinning).

In a similar fashion, the critical level of solution *Wi* number for the FENE-P (Wi_{crit}=2.5) appears earlier than for the LPTT (Wi_{crit}=3.5). Here, and in this limiting instance of shear-thinning behaviour, FENE-P

shows a significant decline in drag up to *Wi*=1.0 (due to its slightly lower η_s at low rates), as compared against the performance of other shear-thinning models (LPTT and EPTT). Nevertheless, over the larger elasticity range $2 \leq Wi \leq 2.5$, findings ultimately tend to coincide, as all three shear-thinning models approach practically the same levels of drag (Figure 4, $\beta_{\text{solvent}}=1/9$).

4.2 ***Drag for dissipative models***: swanINNFM(q) [sIq] - FENE-CR, FENE-P (L=5), LPTT, EPTT ($\varepsilon_{PTT}=0.042$) ($\beta_{\text{solvent}}=0.9, 1/9$), ($\lambda_D=0.0, 0.1, 0.2$) (Figure 5)

High-solvent ($\beta_{\text{solvent}}=0.9$) findings, dissipative: Next, one proceeds by comparison to consider drag response amongst the four counterpart dissipative-viscoelastic swanINNFM(q) [sIq] models, first for high-solvent category fluids. As such, Figure 5 displays *drag* outcome for the four possible candidates from the class of swanINNFM(q) models, with three values of λ_D, the dissipative extensional-viscous material time-scale $\lambda_D=\{0.0, 0.1, 0.2\}$. Mesh refined drag-solutions are also included in Figure 5a,e, for [sIq]-FENE-CR]-($\lambda_D=0.2$), drawing upon coarse, medium and refined meshing levels. This data indicates the overall consistency of such solutions in drag, and the acceptable quality of solution representation under the medium mesh, adopted henceforth [e.g. see 31, 33]. This evidence is further supported with normal stress configuration-difference data (A_{11}-A_{22}), extracted along the centreline of the flow over the associated three levels of refinement. Again this confirms solution consistency and trends, as above, with close agreement upheld, bar from the anticipated localised differences near the stress peak, where stronger gradient representation is influenced by mesh location and spacing, that vary from mesh to mesh.

For each model in turn, the key distinguishing features to discern are: the relative rise in drag above the ($\lambda_D=0.0$)-level; the location of minimum drag (in *Wi*), upturn or plateau behaviour; detection of an intercept with the *Unity-Newtonian reference* and subsequent extent of drag-rise (drag-enhancement). As above, all [sIq]-($\lambda_D=0.0$) forms, display limiting drag correction factor ($\mathrm{K}/\mathrm{K}_{\mathrm{N}}$) asymptotic behaviour (no minima/upturn), with drag-reduction values at *Wi*=6 of {0.97, 0.93, 0.93, 0.93} for variants {FENE-CR, FENE-P, LPTT, EPTT}.

The general finding for all four models with ($\lambda_D>0.0$) is as follows. When increasing beyond base-form, to larger values of first, $\lambda_D=0.1$, then $\lambda_D=0.2$, the trend-in-drag of an *initial-decrease* and *second-increase* can be appreciated. Overall, [sIq]-FENE-CR provides larger drag outcomes against comparable shear-thinning alternatives. So certainly, the inclusion of shear-thinning is reflected in the

lowering of drag levels. Comparing drag findings across shear-thinning variants - trends for [sIq]-FENE-P largely mimic those for [sIq]-LPTT; whilst sIq-EPTT can produce large drag levels, only slightly suppressed from [sIq]-FENE-CR (due to η_e -suppression), with strong drag-enhancement displayed under λ_D =0.2. The explanation for such flow response, lies in η_e -behaviour and the larger protracted deformation-rate ranges accessible for [sIq]-{FENE-CR, EPTT}, which are prematurely stunted under [sIq]-{FENE-P, LPTT} variants, with their earlier solution termination properties. Here, the lack of shear-thinning of the [sIq]-FENE-CR form is the only discernible rheological difference from [sIq]-{FENE-P, LPTT}, that all share close response in η_e. Note, there is no departure from equivalent-model base-form response in N_1 in any of these model instances, that all share common behaviour at low deformation-rates of $\lambda\dot{\gamma} < O(5)$, see Figure 1.

Specifically on (λ_D =0.1) data, sIq-FENE-CR drag (Figure 5a) intercepts the *Unity-Newtonian reference line* (red line) at *Wi*=4; a feature suppressed under all three alternative shear-thinning fluids, providing – no intercept with [sIq]-{FENE-P, LPTT}, and delayed intercept at *Wi*=6 under [sIq]-EPTT, the strain-hardening/softening/hardening variant (Figures 5b-d).

For larger dissipative parameter (λ_D =0.2), sIq-FENE-CR drag intercepts the *Newtonian reference* somewhat earlier, at *Wi*=1. Comparably, at this relatively low-level of *Wi*=1, drag-values for shear-thinning models of [sIq]-{FENE-P, LPTT, EPTT} are almost {4%, 3%, 3%} below unity-reference (manifesting *drag-reduction*). Reporting on maximum drag-outcome, for [sIq]-FENE-CR(λ_D =0.2) - this proves to be significant, with 25% drag-enhancement at *Wi*=6. This is almost replicated with sIq-EPTT(λ_D =0.2), in 20% at *Wi*=6. In stark contrast for [sIq]-{FENE-P, LPTT}, drag-enhancement is hugely stunted to ~3%, as argued above, generating 3% for [sIq]-FENE-P(λ_D =0.2) at *Wi*=3.5, and 2% for [sIq]-LPTT(λ_D =0.2) at *Wi*=3.

On limiting Wi_{crit} and solution convergence with (λ_D >0.0):- [sIq]-FENE-P reaches Wi_{crit}~3.5 for both λ_D =0.1 and λ_D =0.2 solutions. Similarly for [sIq]-LPTT, Wi_{crit}={5.0, 3.0} for λ_D ={0.1, 0.2}. Whilst, [sIq]-{FENE-CR, EPTT} forms do not encounter a limit for *Wi*≤6 (see Table 2a).

Low-solvent ($\beta_{solvent}$ =1/9) findings, dissipative: Figure 6 presents counterpart dissipative drag-data for low-solvent, high-solute fluids. At this level of high-polymeric concentration, the drag-data for all *sIq*-models reflect significant drag-reduction only; lying well below the *Unity-Newtonian* reference line,

with barely any distinction from base-level (λ_D=0)-response, as reported above. The only prominent feature is the earlier Wi_{crit} encountered, under shear-thinning options and with λ_D–rise per model. In the low-solvent context, these findings can be related to extensional viscosity properties relative to all four models, which follow the base-models (λ_D=0.0). Here, there is absence of sharp departure in η_e from base-form response until larger rates of ~10 are reached, see Figure 2. This stands in direct contrast to the high-solvent context, described above, where such departure in extensional viscosity properties appears a decade earlier in rate.

5. Drag Results for alternative geometries: $\beta_{\text{sphere}} = 0.4$ **and** $\beta_{\text{sphere}} = 0.2$

5.1 Fixed geometry: $\beta_{\text{sphere}} = 0.4$

swanINNFM(q) [sIq]-FENE-CR(L=5), LPTT, EPTT (ε_{PTT}=0.042) models) : Corresponding drag results are presented in Figure 7 for the alternative medium-fit aspect-ratio $\beta_{\text{sphere}} = 0.4$. One can proceed here by addressing drag-outcomes for each model in turn, [sIq]-{FENE-CR, LPTT, EPTT}, and with direct back-reference to the tighter-fit aspect-ratio results for ($\beta_{\text{sphere}} = 0.5$) per model. In this, the common reference for Weissenberg number interpretation is retained, as that based on $\beta_{\text{sphere}} = 0.5$, but with the *adjustment to U/a* required by the *length-scale switch*

First for **{**$\beta_{\text{sphere}} = 0.4$**,** $\beta_{\text{solvent}} = 0.9$}: In Figure 7, and for with [sIq]-FENE-CR, the only noticeable feature is a down-shift in drag-enhancement: at λ_D=0.2 to { K/K_N =1.18, *Wi*=4.8}, representing {25%, $\beta_{\text{sphere}} = 0.5$} to (18%, $\beta_{\text{sphere}} = 0.4$}; at λ_D=0.1 to { K/K_N =1.03, *Wi*=4.8}, representing {5%, $\beta_{\text{sphere}} = 0.5$} to (3%, $\beta_{\text{sphere}} = 0.4$}. With modest up-shift in drag-reduction at λ_D=0.0 to { K/K_N =0.97, *Wi*=4.8, -3%, $\beta_{\text{sphere}} = 0.4$} from { K/K_N =0.96, *Wi*=6.0, -4%, $\beta_{\text{sphere}} = 0.5$}.

Next turning to sIq-LPTT, the most outstanding feature of contrast in aspect-ratio adjustment is the impact on *drag-upturn* and *rate-of-rise* subsequently: at λ_D=0.0 *upturn* occurs at { K/K_N =0.92, Wi_{up}=2.6}, rising to { K/K_N =0.98, Wi_{crit}=4.8}, representing drag-reduction of {-8%, $\beta_{\text{sphere}} = 0.5$} to {-2%, $\beta_{\text{sphere}} = 0.4$}; at λ_D=0.1 *upturn* occurs at { K/K_N =0.95, Wi_{up}=2.5}, *intercept* at Wi_{inter}=4.0, rising to { K/K_N =1.03, Wi_{crit}=4.4}, representing drag-reduction of {-4%, $\beta_{\text{sphere}} = 0.5$, Wi_{crit}=5.0} to drag-enhancement of {3%, $\beta_{\text{sphere}} = 0.4$, Wi_{crit}=4.4}; at λ_D=0.2 premature early termination occurs

prior to upturn at { K/K_N =0.98, Wi_{crit}=2.0} for $\beta_{sphere} = 0.4$, in contrast to upturn, intercept and enhancement for $\beta_{sphere} = 0.5$.

The third model [sIq]-EPTT, shows only minor change with aspect-ratio adjustment, and that only for the largest value of λ_D =0.2, with *upturn* delayed to around Wi_{up}=1.5 and *intercept* at Wi_{inter}=2.3 (Wi_{up}=1.0, Wi_{inter}=2.5, previously with $\beta_{sphere} = 0.5$). Here, only modest down-shift in drag-enhancement is noted from { K/K_N =1.21, $\beta_{sphere} = 0.5$, Wi_{crit}=6} to { K/K_N =1.16, $\beta_{sphere} = 0.4$, Wi_{crit}=4.8}. At λ_D =0.1, the drag coefficient now lies marginally below the Newtonian reference { K/K_N =0.996, $\beta_{sphere} = 0.4$, Wi_{crit}=4.8}.

On data for { $\beta_{sphere} = 0.4$, $\beta_{sphere} = 0.2$, $\beta_{solvent} = 1/9$ }: In the high-solute context, and for λ_D ={0.0-0.2} across the [sIq]-models, only drag reduction is observed with little change across λ_D-data, with only slight up-shift in drag from ($\beta_{sphere} = 0.5$) to ($\beta_{sphere} = 0.4$) to $\beta_{sphere} = 0.2$ case; see Table 2b-c.

5.2 Fixed geometry $\beta_{sphere} = 0.2$

swanINNFM(q) [sIq]-FENE-CR(L=5), LPTT, EPTT(ε_{PTT} =0.042) models) : As above, drag data with still further reduction in aspect ratio to $\beta_{sphere} = 0.2$, is provided in Figure 8. Here, there are mixed findings to review over the λ_D-data analysed. An overall summary from $\beta_{sphere} = 0.4$ to $\beta_{sphere} = 0.2$ would indicate the following. With $\beta_{solvent}$=0.9, and for [sIq]-{FENE-CR, EPTT}, λ_D ={0.0, 0.1}-data are slightly elevated, whilst limiting { K/K_N , λ_D =0.2}-data is reduced by about 10%. Turning to [sIq]-LPTT, in λ_D ={0.0, 0.1}-data no data upturn is detected, in fact is replaced with limiting downturn. Correspondingly with (λ_D =0.2)-data, the declining-to-flat drag-trend of $\beta_{sphere} = 0.4$, is completely adjusted to $\beta_{sphere} = 0.2$, now showing upturn, intercept (Wi_{up}=0.48, Wi_{inter}=1.0), and drag-enhancement with limiting { K/K_N =1.009, Wi_{crit}=1.34}.

5.3 Comparison across geometry aspect-ratios: $0.2 \le \beta_{sphere} \le 0.5$

Garduño *et al.* [1], provides drag-data that tightly matches the Boger Fluid experimental data of Jones *et al*. [8]. This is extracted with the single [sIq]-FENE-CR (Boger-like, constant viscosity model) *under variable dissipative time-scale* ($0.35 \le \lambda_D \le 0.62$), and across each of the three geometric aspect-

ratios (see also, Figure 9a with λ_D=0.2). Accordingly, one notes the general trend, that for smaller β_{sphere} values, larger λ_D -values are required to match the more exaggerated experimental drag-correction measurements. One may refer to Garduño *et al.* [1], Jones *et al.* [8] and Arigo *et al.* [17] for more detail and discussion on - the impact of settling velocity and its adjustment, downstream wake, stagnation-point dynamics, early drop below Newtonian drag, and thus, ultimate drag outcome at larger rates. Note, that an early drop below the Newtonian drag-level is apparent for β_{sphere}>0.4, as reported in [15].

Figure 9 provides a direct summary on the *fixed* maximum (λ_D=0.2) data, over all three geometry aspect-ratios, provided per model and for the more responsive high-solvent $\beta_{solvent}$=0.9 instance. Here, suitable scaling is required to retain consistency across the geometric aspect-ratios, on relative drag-values (K_N) and Weissenberg number interpretation. As a consequence, it is clearly apparent, that increase in aspect-ratio in the range $0.2 \le \beta_{sphere} \le 0.5$, generally provides suppression in drag coefficient across the deformation-rate range.

Note, on raw drag of Figure 10, for a fixed value of λ_D=0.2, the converse is true. Here, for the three different and increasing geometry aspect-ratios, the elevated differences in raw drag values are clearly apparent. Such raw drag data now lies in distinct contrast against the drag correction factors (K/K_N) reported in Figure 9a. One notes that, the computed values of Stokesian drag force used are given by K_N={5.931, 3.592, 1.688} for β_{sphere}={0.5, 0.4, 0.2}, see also Happel and Brenner [36].

Yet on terminating drag correction factor, this still leads to overall drag-enhancement. Such an observation is upheld ultimately for [sIq]-{FENE-CR, EPTT}, with some early-rate switch-over occurring, that is more prominent with [sIq]-EPTT. Additionally, the [sIq]-LPTT data does indicate significant drag cross-over with the $\beta_{sphere} = 0.4$ geometry.

6. Conclusions

This analysis begins with comparison against base-level, null-dissipative (λ_D=0.0), drag findings over two levels of fluid solvent-fraction. There, high-solvent/low-solute ($\beta_{solvent}$=0.9) *drag coefficient* reached around ~3% drag-reduction for constant-viscosity FENE-CR; the drop doubles to ~7%, for the

shear-thinning FENE-P and PTT models. This would indicate that high-solvent options do not enter deformation-rate regimes of rheological distinction, compared to their *low-solvent* counterparts. In contrast, low-solvent/high-solute (β_{solvent}=1/9) solutions show considerably more pronounced decline in *drag* than for their *high-solvent* counterparts. Noticeably, the exponential PTT (EPTT) model, with its *strain-hardening/softening* properties, provides a much wider solution-range of elasticity (up to *Wi*=6).

Advancing to consider dissipative model findings: Under ***high-solvent*** (β_{solvent}=0.9) systems and for each model in turn, the key distinguishing features to discern are: the relative rise in drag above the (λ_D=0.0)-level; the location of minimum drag (in *Wi*), upturn or plateau behaviour; detection of an intercept with the *Newtonian reference-line* and subsequent extent of drag-rise (drag-enhancement). The general observation for all four models with (λ_D>0.0), is that by increasing beyond base-form, to larger values of λ_D=0.1 and λ_D=0.2, produces an *initial-decrease* and subsequent *second-increase* for trend-in-drag. The sIq-FENE_CR fluid data (devoid of shear-thinning, Fig.5a), indicates that a high-solvent system would response similarly in trend to a (generalized) Newtonian fluid, but that as extensional dissipation is gradually introduced (via λ_D), extensional stress contributions (viscous dominant over polymeric) raise drag expectations to match those found experimentally for Boger fluids. Overall, the inclusion of shear-thinning is reflected in the lowering of drag levels. Comparing drag findings across shear-thinning variants - trends for [sIq]-FENE-P largely mimic those for [sIq]-LPTT; whilst [sIq]-EPTT can produce large drag levels, only slightly suppressed from [sIq]-FENE-CR (due to η_e-suppression), with strong drag-enhancement displayed under λ_D=0.2. The explanation for such flow response, lies in η_e-behaviour and the larger protracted deformation-rate ranges accessible for [sIq]-{FENE-CR, EPTT}; which are equivalently and prematurely stunted under [sIq]-{FENE-P, LPTT} variants, with their earlier solution termination properties. One notes, in the case of [sIq]-FENE-CR, the only discernible rheological difference from [sIq]-{FENE-P, LPTT}, is its lack of shear-thinning.

For low-solvent **(**β_{solvent}=1/9) counterpart dissipative systems - all *sIq*-models reflect only significant drag-reduction, with barely any distinction from base-level (λ_D=0)-response, consistent in form to that frequently reported in the computational literature for this solvent-fraction range. Here, even though one might expect drag enhancement, with more dominant polymeric over viscous stress contributions, extensional contributions do not impact strongly enough at the rates reported. The explanation for this low solvent-fraction finding, is due to the absence of sharp departure in η_e from base-level response,

until significantly larger rates of $O(10)$ have been reached. One also notes the early stunting of solutions to Wi~3 (bar under sIq-EPTT). This observation stands in *distinct contrast* to that *for high solvent-fraction systems*, where such η_e-departure occurs at rates that are one order lower ($O(1)$ units).

Adjustment over three geometric aspect-ratios: Over all three geometry aspect-ratios studied in the range $0.2 \le \beta_{\text{sphere}} \le 0.5$, a direct summary on the *fixed* maximum (λ_D=0.2)-data and for high-solvent β_{solvent}=0.9 instance, indicates that *increase* in aspect-ratio, generally provokes suppression of drag coefficient across the deformation-rate range; yet the overall evidence leads to stimulating *ultimate* drag-enhancement with rising rate. In particular, under the shear-thinning/strain-hardening-softening [sIq]-EPTT option, there is evidence for *relatively pronounced drag-enhancement*, with only modest down-shift from that produced by the constant-viscosity [sIq]-FENE-CR model. To gather more precise matching to experimental drag-levels across geometric aspect-ratios, experience would indicate that a *variable dissipative time-scale* λ_D *is required*, suitably elevated to reach the more exaggerated drag levels of the experiments.

Experimental data are presently not readily available on the falling sphere problem for *shear-thinning* viscoelastic fluids. Hence as such, much work on this problem yet remains outstanding, to attain truly quantitative agreement with experiments. The present study stands as a significant predictive step forward towards this ultimate goal.

Acknowledgements

I.E. Garduño gratefully acknowledges the financial support from Consejo Nacional de Ciencia y Tecnología (Mexico) through scholarship No. 310618. Thanks also to our colleagues within the INNFM Wales UK, for their help and support throughout this work, but particularly to Professor Ken Walters, FRS.

Dedication from I.E. Garduño and colleagues in INNFM Wales, UK

This work has been written and dedicated to the memory of an exceptional young Mexican rheologist, Dr. Víctor Hugo Rolón Garrido. There is no doubt that to lose a close relative, or friend, is something hard to come to terms with. The passing of Víctor Hugo, without doubt was a painful lose, not only to his family, wife and daughter, but also to those that shared the privilege of meeting him. Dr. Rolón-Garrido left a considerable legacy as a friend, colleague and through his work to the science of rheology. He will be sadly missed.

References

[1] I.E Garduño, H.R. Tamaddon-Jahromi, M.F. Webster, The falling sphere problem and capturing enhanced drag with Boger fluids, J. Non-Newton. Fluid Mech. 231 (2016) 26–48

[2] M. Chilcott, J. Rallison, Creeping flow of dilute polymer solutions past cylinders and spheres, J. Non-Newton. Fluid Mech. 29 (1988) 381–432.

[3] J.L. White, A.B. Metzner, Development of constitutive equations for polymeric melts and solutions, J. Appl. Polym. Sci. 7(1963) 1867–1889.

[4] H.R. Tamaddon-Jahromi, I.E. Garduño, J.E. López-Aguilar, M.F. Webster, Predicting Excess pressure drop (epd) for Boger fluids in expansion-contraction flow, J. Non-Newton. Fluid Mech. 230 (2016) 43–67.

[5] J.E. López-Aguilar, H.R. Tamaddon-Jahromi, M.F. Webster, K. Walters, Numerical vs experimental pressure drops for Boger fluids in sharp-corner contraction flow, Physics of Fluids 28 (2016).

[6] H.R. Tamaddon-Jahromi, M.F. Webster, P.R. Williams, Excess pressure drop and drag calculations for strain-hardening fluids with mild shear-thinning: Contraction and falling sphere problems, J. Non-Newton. Fluid Mech. 166 (2011) 939–950.

[7] N. Phan-Thien, R.I. Tanner, A new constitutive equation derived from network theory, J. Non-Newton. Fluid Mech. 2 (1977) 353–365.

[8] W. Jones, A. Price, K. Walters, The motion of a sphere falling under gravity in a constant-viscosity elastic liquid, J. Non-Newton. Fluid Mech. 53 (1994) 175–196.

[9] K. Walters, R.I. Tanner, The motion of a sphere through an elastic fluid, *in R.P. Chhabra and D. De Kee (Eds.), Transport processes in Bubbles, Drops and Particles* (1992)73-86.

[10] R.G. Owens, T.N. Phillips, *Computational Rheology*, Imperial College Press, (2002) London

[11] R.I. Tanner, Engineering Rheology, 2nd ed., (2000) Oxford

[12] G.H. McKinley, Steady and transient motion of spherical particles in viscoelastic liquids, *in R.P. Chhabra, D. De Kee (Eds.), Transport Processes in Bubbles, Drops and Particles,* Taylor & Francis, (2001) New York.

[13] S. Chen, J.P. Rothstein, Flow of a wormlike micelle solution past a falling sphere, J. Non-Newton. Fluid Mech. 116 (2004) 205–234.

[14] P.M. Coelho, F.T. Pinho, Vortex shedding in cylinder flow of shear-thinning, J. Non-Newton. Fluid Mech., 121 (2004) 55–68.

[15] A.J. Mendoza-Fuentes, O. Manero, R. Zenit, Evaluation of drag correction factor for spheres settling in associative polymers, Rheologica Acta. 49 (2010) 979–984

[16] R.P. Chhabra, P.H.T. Uhlherr, The influence of fluid elasticity on wall effects for creeping sphere motion in cylindrical tubes, Can. J. Chem. Eng. 66 (1988) 154–157.

[17] M.T. Arigo, D. Rajagopalan, N. Shapley, G.H. McKinley, The sedimentation of a sphere through an elastic fluid. Part 1. Steady motion, J. Non-Newt. Fluid Mech., 60 (1995) 225–257

[18] L.E. Becker, G.H. McKinley, H.K. Rasmussen, O. Hassager, The unsteady motion of a sphere in a viscoelastic fluid, J. Rheol. 38 (1994) 377–403.

[19] H.K. Rasmussen, O. Hassager, On the sedimentation velocity of spheres in a polymeric liquid, Chemical Engineering Science. 51 (1996) 1431–1440.

[20] H. Jin, N. Phan-Thien, R.I. Tanner, A finite element analysis of the flow past a sphere in a cylindrical tube: PTT fluid model, Computational Mechanics. 8 (1991) 409–422.

[21] W.J. Lunsmann, L. Genieser, R.C. Armstrong, R.A. Brown, Finite element analysis of steady viscoelastic flow around a sphere in a tube: calculations with constant viscosity models, J. Non-Newton. Fluid Mech. 48 (1993) 63–99.

[22] D. Song, R.K. Gupta, R.P. Chhabra, Effects of Shear-thinning and Elasticity in Flow around a Sphere in a Cylindrical Tube, Proceedings of the COMSOL Conference (2010).

[23] R. Zheng, N. Phan-Thien, R.I. Tanner, On the flow past a sphere in a cylindrical tube: limiting Weissenberg number, J. Non-Newton. Fluid Mech. 36 (1990) 27–49.

[24] R. Zheng, N. Phan-Thien, R.I. Tanner, The flow past a sphere in a cylindrical tube: effects of inertia, shear-thinning and elasticity, Rheologica Acta. 30 (1991) 499–510.

[25] A. Abedijaberi, B. Khomami, Sedimentation of a sphere in a viscoelastic fluid: a multiscale simulation approach, J. of Fluid Mech. 694 (2012) 78–99.

[26] K.D. Housiadas, R.I. Tanner, A high-order perturbation solution for the steady sedimentation of a sphere in a viscoelastic fluid, J. Non-Newton. Fluid Mech. 233 (2016) 166–180.

[27] J.E. López-Aguilar, M.F. Webster, H.R. Tamaddon-Jahromi, O. Manero, High-Weissenberg predictions for micellar fluids in contraction–expansion flows, J. Non-Newton. Fluid Mech. 222 (2015) 190–208.

[28] López-Aguilar, J.E., Webster, M.F., Tamaddon-Jahromi, H.R., and Manero O. "Convoluted

models & high-Weissenberg predictions for micellar thixotropic fluids in contraction-expansion flows", J. Non-Newton. Fluid Mech. (2016) 232 55–66.

[29] H.R. Tamaddon-Jahromi, F.S. Syed, M.F. Webster, Studies on Contraction Flows and Pressure-Drops-Extensional Viscosity and Dissipative Stress Effects, in: XVth International Congress on Rheology, AIP, Monterey, CA, (2008) pp. 225–227.

[30] E.O.A. Carew, P. Townsend, M.F.Webster, A Taylor-Petrov-Galerkin algorithm for viscoelastic flow, J. Non-Newton. Fluid Mech, 50 (1993) 253–287.

[31] P. Wapperom, M.F. Webster, A second-order hybrid finite-element/volume method for viscoelastic flows, J. Non-Newton. Fluid Mech. 79 (1998) 405–431.

[32] M. Aboubacar, M.F. Webster, A cell-vertex finite volume/element method on triangles for abrupt contraction viscoelastic flows, J. Non-Newton. Fluid Mech. 98 (2001) 83–106.

[33] M.F. Webster, H.R. Tamaddon-Jahromi, M. Aboubacar, Transient viscoelastic flows in planar contractions. J. Non-Newton. Fluid Mech., 118 (2004) 83–101.

[34] F. Belblidia, H. Matallah, B. Puangkird, M.F. Webster, Alternative subcell discretisations for viscoelastic flow: Stress interpolation, J. Non-Newton. Fluid Mech. 146 (2007) 59-78.

[35] F. Belblidia, H. Matallah, M.F. Webster, Alternative subcell discretisations for viscoelastic flow: Velocity-gradient approximation, J. Non-Newton. Fluid Mech. 151 (2008) 69-88.

[36] J. Happel, H. Brenner, Low Reynolds number hydrodynamics, 2nd edition, (1973) Noordhoff International Publishing, Leyden.

Figure captions

Table 1. Mesh characteristics: different sphere aspect ratios, $\beta_{sphere}=a/R=0.5$ (coarse, medium, refined), $\beta_{sphere}=0.4$, $\beta_{sphere}=0.2$

Table 2a. Drag correction factor (K/K_N *max*), various λ_D, $\beta_{solvent}=0.9$, 1/9, $\beta_{sphere}=0.5$

Table 2b. Drag correction factor (K/K_N *max*), various λ_D, $\beta_{solvent}=0.9$, 1/9, $\beta_{sphere}=0.4$

Table 2c. Drag correction factor (K/K_N *max*), various λ_D, $\beta_{solvent}=0.9$, 1/9, $\beta_{sphere}=0.2$

Fig 1. Material functions, **base-models,** a) $\boldsymbol{\beta_{solvent}=0.9}$, b) $\boldsymbol{\beta_{solvent}=1/9}$

Fig 2. Extensional viscosity; **base and [sIq]-models**

Fig 3. a) Schematic diagram, flow past a sphere geometry; mesh patterns around sphere: b) $\beta_{sphere}=a/R=0.5$, $\beta_{sphere}=0.4$, $\beta_{sphere}=0.2$ c) $\beta_{sphere}=a/R=0.5$, coarse, medium, and refined

Fig 4. Drag correction factor $\beta_{sphere}=0.5$, **base-models**

Fig 5a-d. Drag correction factor $\boldsymbol{\beta_{sphere}=0.5}$, $\beta_{solvent}=0.9$; dissipative [sIq]-models, $0.0\leq\lambda_D\leq0.2$;

——— Newtonian reference

Fig 5e. (A_{11}-A_{22}) at centerline (refined, medium, coarse meshes), dissipative [sIq]-models, $\lambda_D=0.2$

Fig 6. Drag correction factor $\boldsymbol{\beta_{sphere}=0.5}$, $\beta_{solvent}=1/9$; dissipative [sIq]-models, $0.0\leq\lambda_D\leq0.2$;

——— Newtonian reference

Fig 7. Drag correction factor $\boldsymbol{\beta_{sphere}=0.4}$, $\beta_{solvent}=0.9$; dissipative [sIq]-models, $0.0\leq\lambda_D\leq0.2$

Fig 8. Drag correction factor $\boldsymbol{\beta_{sphere}=0.2}$, $\beta_{solvent}=0.9$; dissipative [sIq]-models, $0.0\leq\lambda_D\leq0.2$

Fig 9. Drag correction factor, $\boldsymbol{\beta_{sphere}}$ **comparison**: dissipative [sIq]-models, $\beta_{solvent}=0.9$, $\lambda_D=0.2$**;**

——— Newtonian reference

Fig 10. Drag (K) values, $\boldsymbol{\beta_{sphere}}$ **comparison**, [sIq]-FENE-CR model, $\lambda_D=0.2$; $\beta_{solvent}=0.9$

Table 1. Mesh characteristics: different sphere aspect ratios, $\beta_{\text{sphere}}=a/R=0.5$ (coarse, medium, refined), $\beta_{\text{sphere}}=0.4$, $\beta_{\text{sphere}}=0.2$

Meshes	Elements	Nodes	Degree of freedom $(\mathbf{u}, p, \tau)$	
$\beta_{\text{sphere}}=0.5$	1600	3381	21177	*coarse*
	2687	5610	35122	*medium*
	7400	15191	95042	*refined*
$\beta_{\text{sphere}}=0.4$	3306	6861	42944	
$\beta_{\text{sphere}}=0.2$	3986	8229	51496	

Table 2a. Drag correction factor (K/K_N *max*), various λ_D, $\beta_{solvent}$=0.9, 1/9, β_{sphere}=0.5

β_{sphere}	Model	$\beta_{solvent}$	λ_D	Wi_{crit}	K/K_N *max*
0.5	[sIq]-FENE-CR	0.9	0.0	6.0	0.9591
			0.1	6.0	1.0528
			0.2	6.0	1.2466
		1/9	0.0	2.5	0.6555
			0.1	2.5	0.7249
			0.2	2.5	0.7056
	[sIq]-FENE-P	0.9	0.0	6.0	0.9287
			0.1	3.5	0.9555
			0.2	3.5	1.0294
		1/9	0.0	2.5	0.4742
			0.1	2.0	0.4549
			0.2	2.0	0.4885
	[sIq]-LPTT	0.9	0.0	6.0	0.9212
			0.1	5.0	0.9583
			0.2	3.0	1.0216
		1/9	0.0	3.5	0.3751
			0.1	2.4	0.4192
			0.2	1.0	0.6726
	[sIq]-EPTT	0.9	0.0	6.0	0.9176
			0.1	6.0	1.0033
			0.2	6.0	1.2138
		1/9	0.0	6.0	0.2841
			0.1	3.5	0.3708
			0.2	1.0	0.7044

Table 2b. Drag correction factor (K/K_N *max*), various λ_D, $\beta_{solvent}$=0.9, 1/9, β_{sphere}=0.4

β_{sphere}	Model	$\beta_{solvent}$	λ_D	Wi_{crit}	K/K_N *max*
0.4	[sIq]-FENE-CR	0.9	0.0	4.8	0.9722
			0.1	4.8	1.0304
			0.2	4.8	1.1832
		1/9	0.0	2.8	0.7293
			0.1	2.8	0.7218
			0.2	2.4	0.6876
	[sIq]-LPTT	0.9	0.0	4.8	0.9860
			0.1	4.4	1.0362
			0.2	2.0	0.9816
		1/9	0.0	1.8	0.4923
			0.1	1.6	0.5251
			0.2	1.6	0.7913
	[sIq]-EPTT	0.9	0.0	4.8	0.9315
			0.1	4.8	0.9962
			0.2	4.8	1.1606
		1/9	0.0	4.8	0.3209
			0.1	4.8	0.3388
			0.2	4.8	0.7799

Table 2c. Drag correction factor (K/K_N *max*), various λ_D, $\beta_{solvent}$=0.9, 1/9, β_{sphere}=0.2

β_{sphere}	Model	$\beta_{solvent}$	λ_D	Wi_{crit}	K/K_N *max*
0.2	[sIq]-FENE-CR	0.9	0.0	4.8	1.0077
			0.1	2.4	1.0321
			0.2	4.0	1.0660
		1/9	0.0	1.4	0.9396
			0.1	1.4	0.9606
			0.2	1.4	0.9521
	[sIq]-LPTT	0.9	0.0	2.4	0.9330
			0.1	2.2	0.9637
			0.2	1.4	1.0086
		1/9	0.0	1.8	0.4792
			0.1	1.4	0.6649
			0.2	1.0	0.8044
	[sIq]-EPTT	0.9	0.0	2.4	0.9462
			0.1	2.4	0.9636
			0.2	2.4	1.0464
		1/9	0.0	2.4	0.4857
			0.1	2.4	0.5349
			0.2	1.2	0.7432

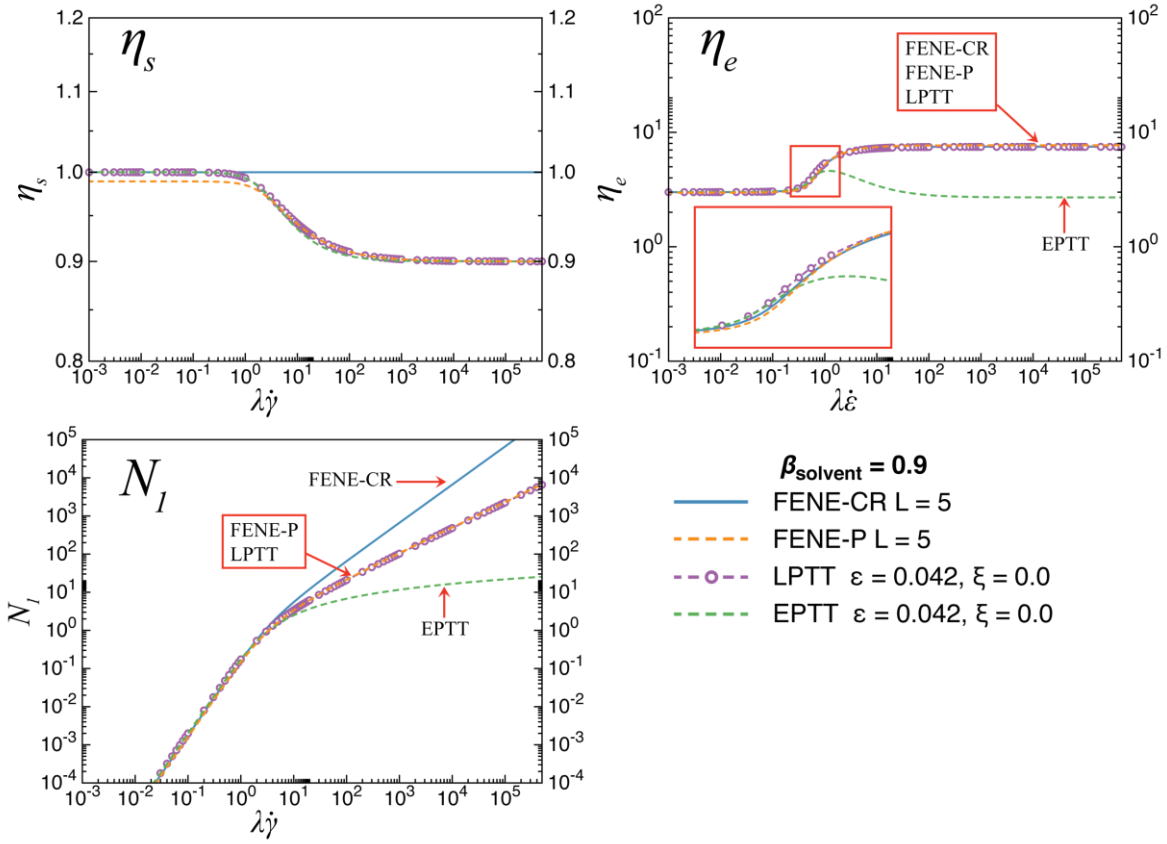

Fig 1a. Material functions, **base-models**; $\beta_{solvent}$**=0.9**

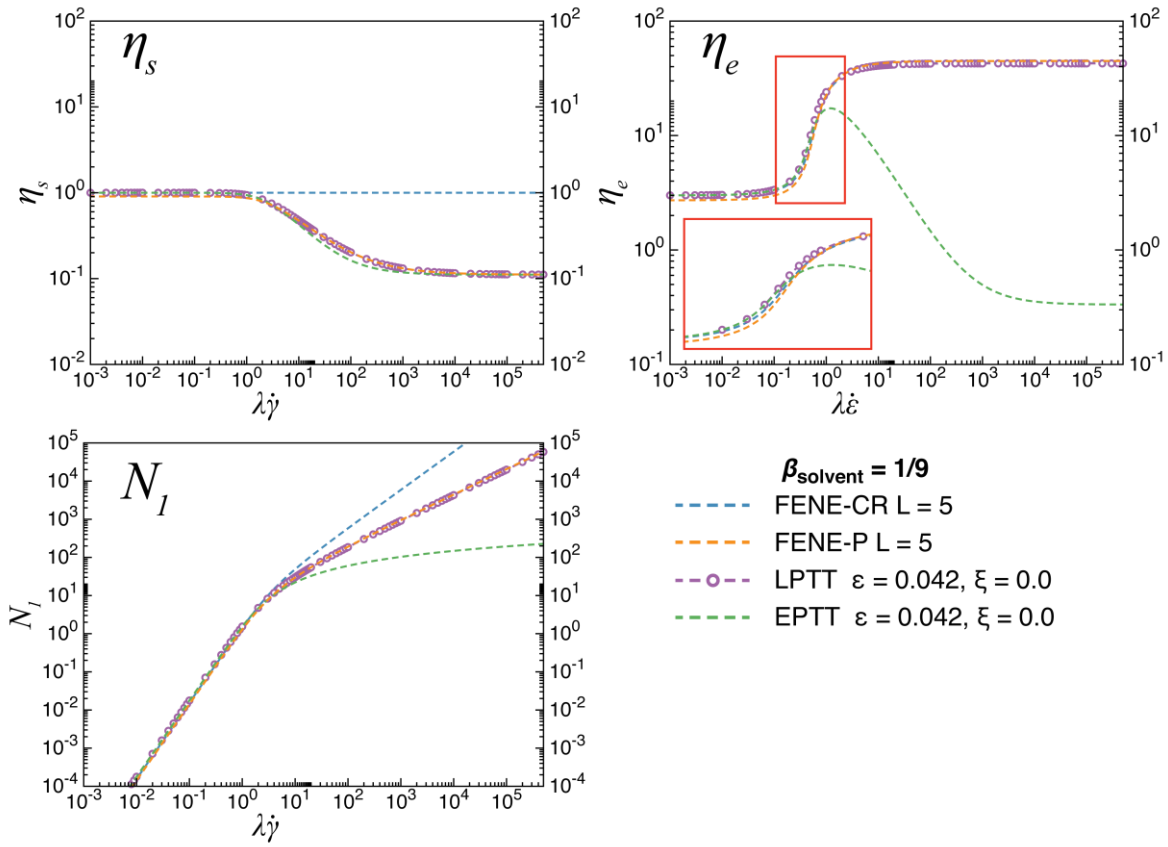

Fig 1b. Material functions, **base-models**; $\beta_{solvent}$**=1/9**

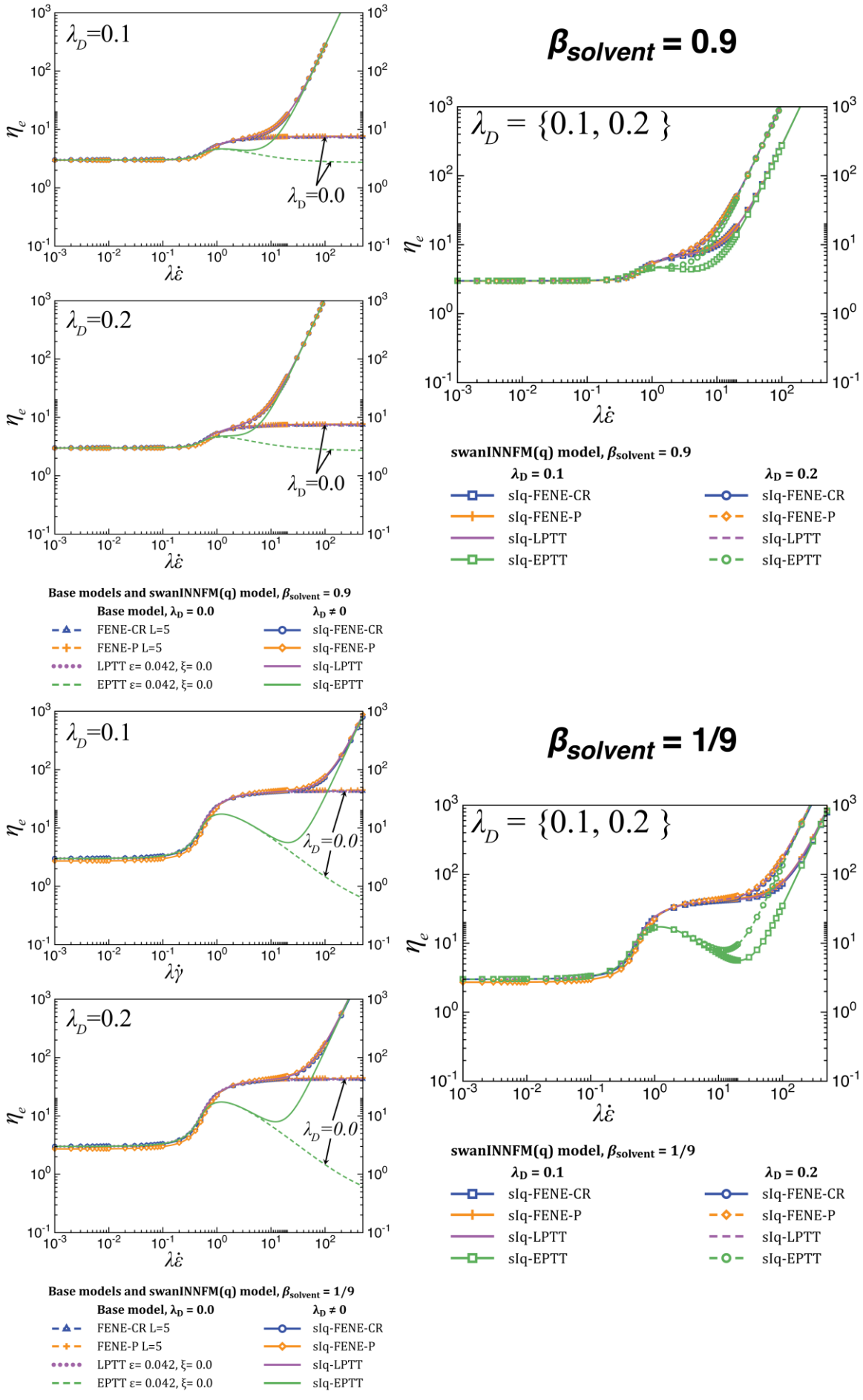

Fig 2. Extensional viscosity; **base and [sIq]-models**

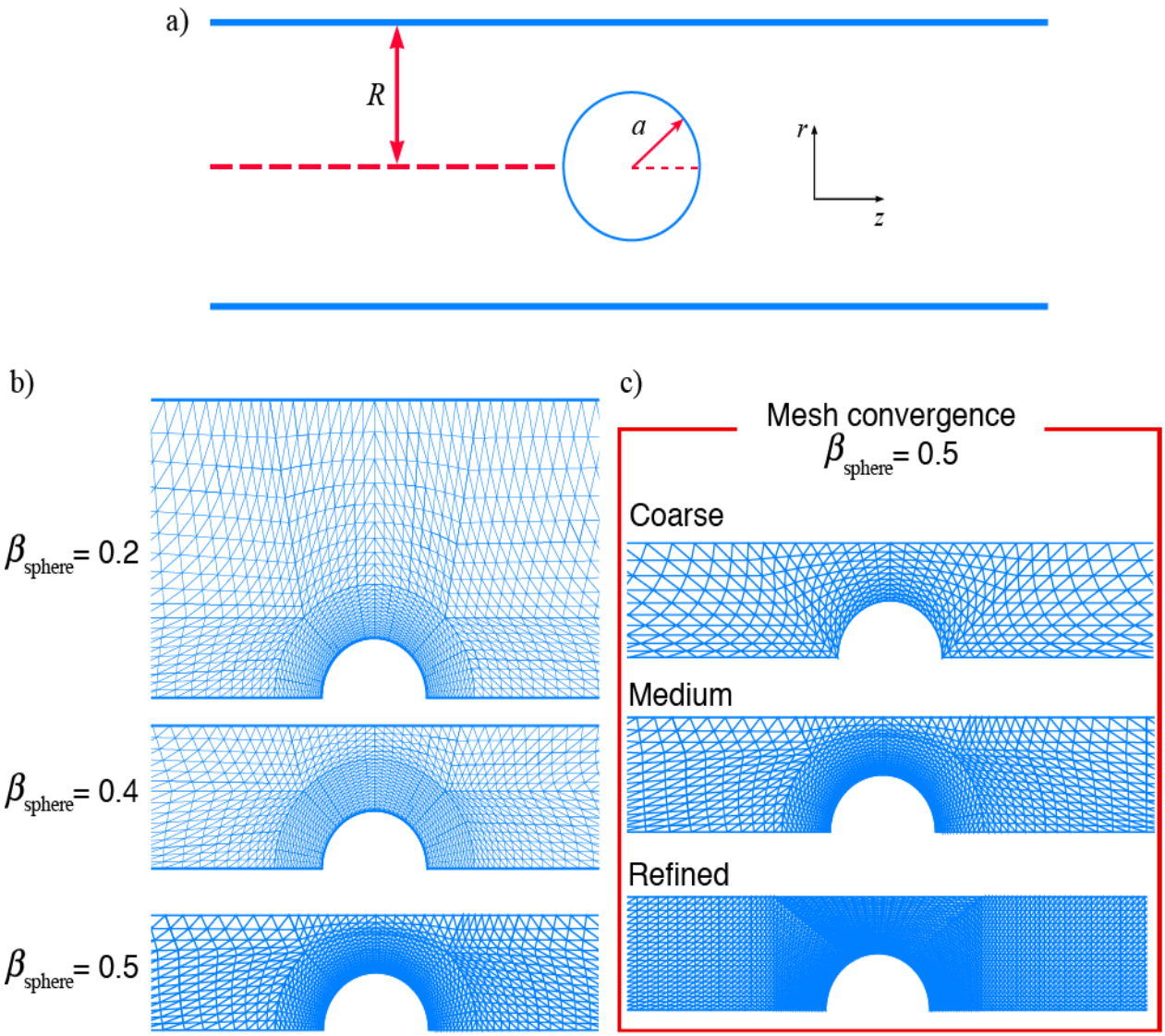

Fig 3. a) Schematic diagram, flow past a sphere geometry; mesh patterns around sphere: b) $\beta_{sphere} = a/R = 0.5$, $\beta_{sphere} = 0.4$, $\beta_{sphere} = 0.2$ c) $\beta_{sphere} = a/R = 0.5$, coarse, medium, and refined

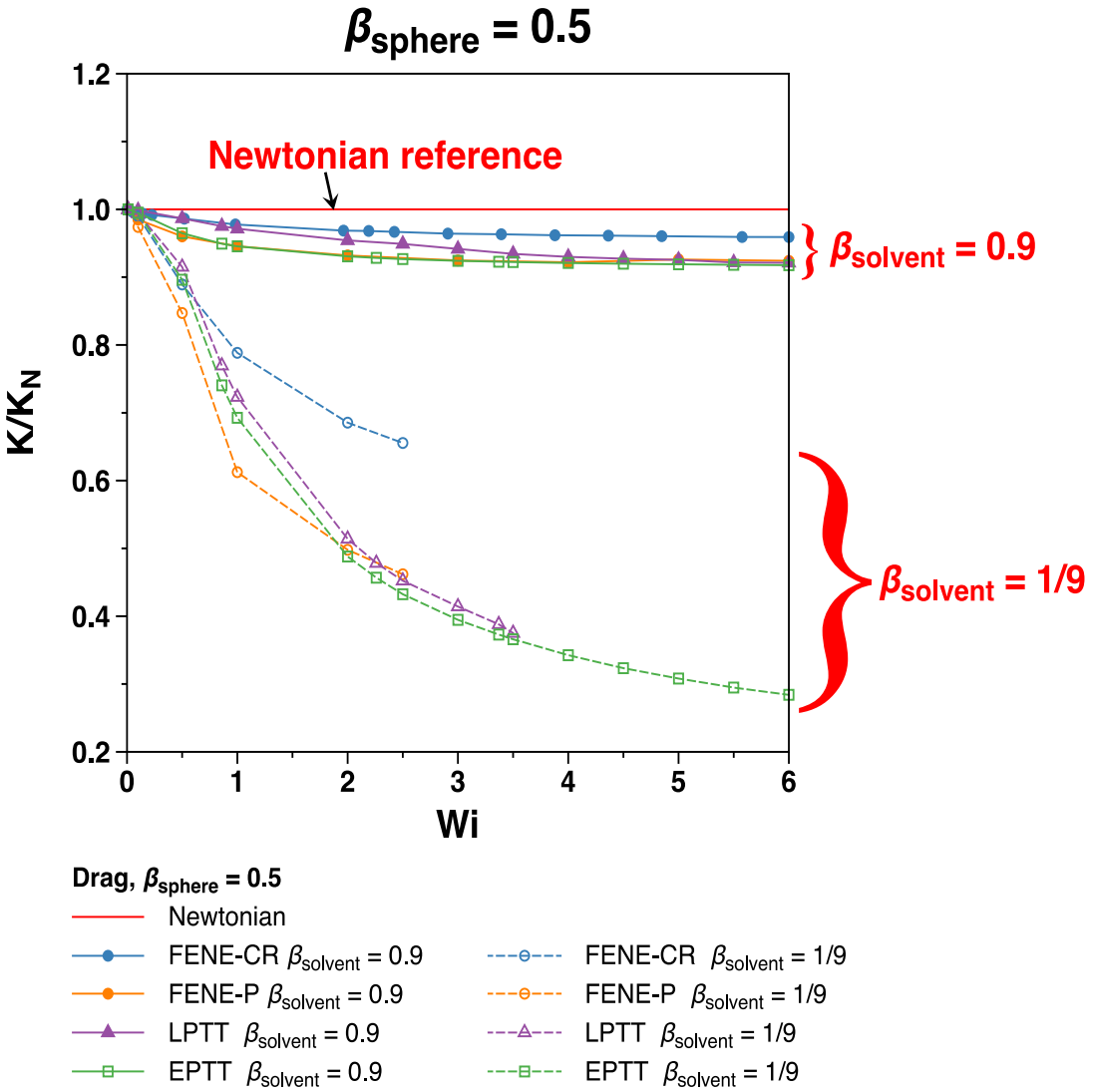

Fig 4. Drag correction factor β_{sphere}=0.5, **base-models**

High-solvent sIq, base-geometry β_{sphere}=0.5

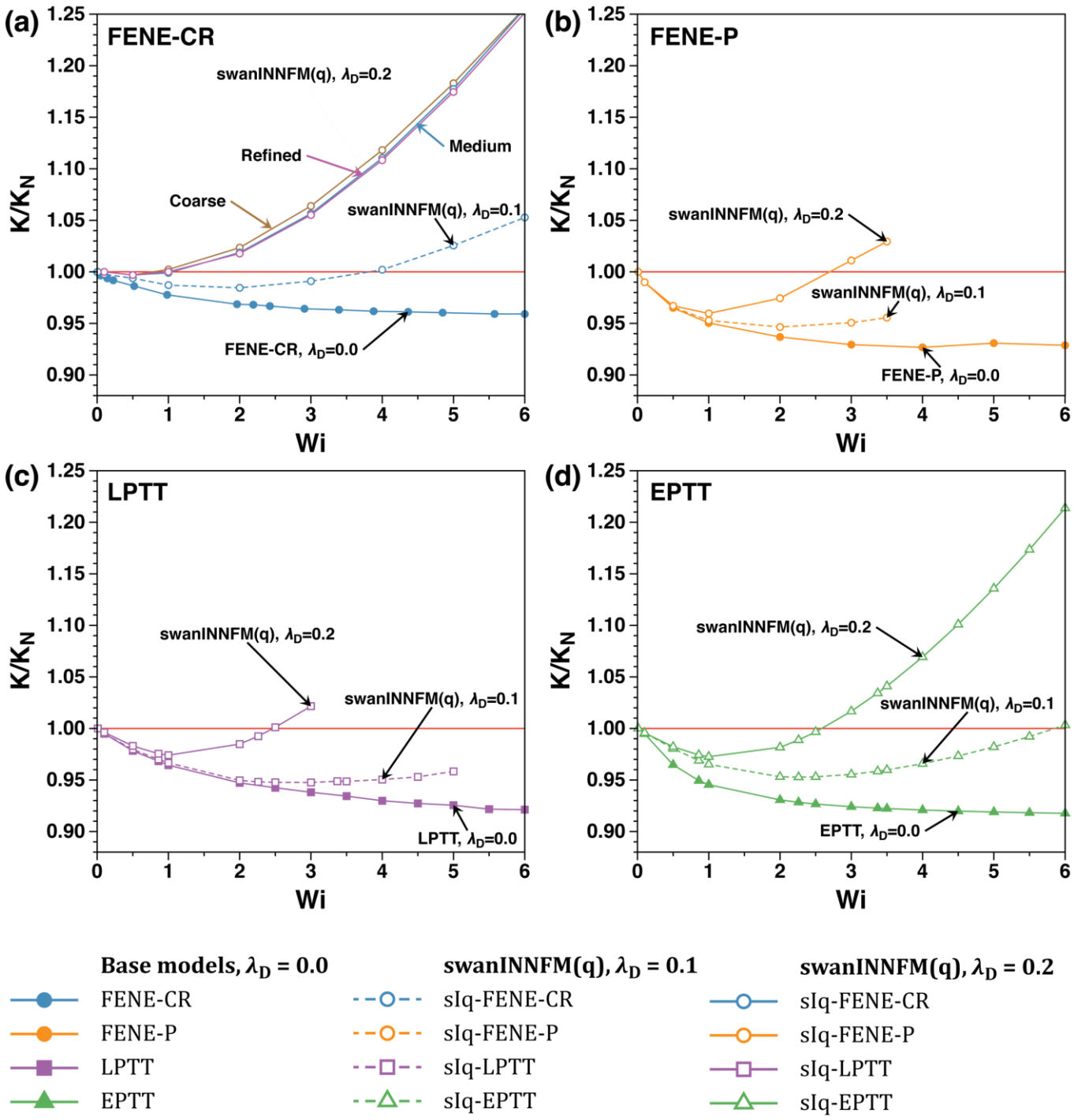

Fig 5a-d. Drag correction factor β_{sphere}**=0.5**, $\beta_{solvent}$=0.9; dissipative [sIq]-models, 0.0≤λ_D≤0.2;

Newtonian reference

High-solvent sIq, base-geometry β_{sphere}=0.5

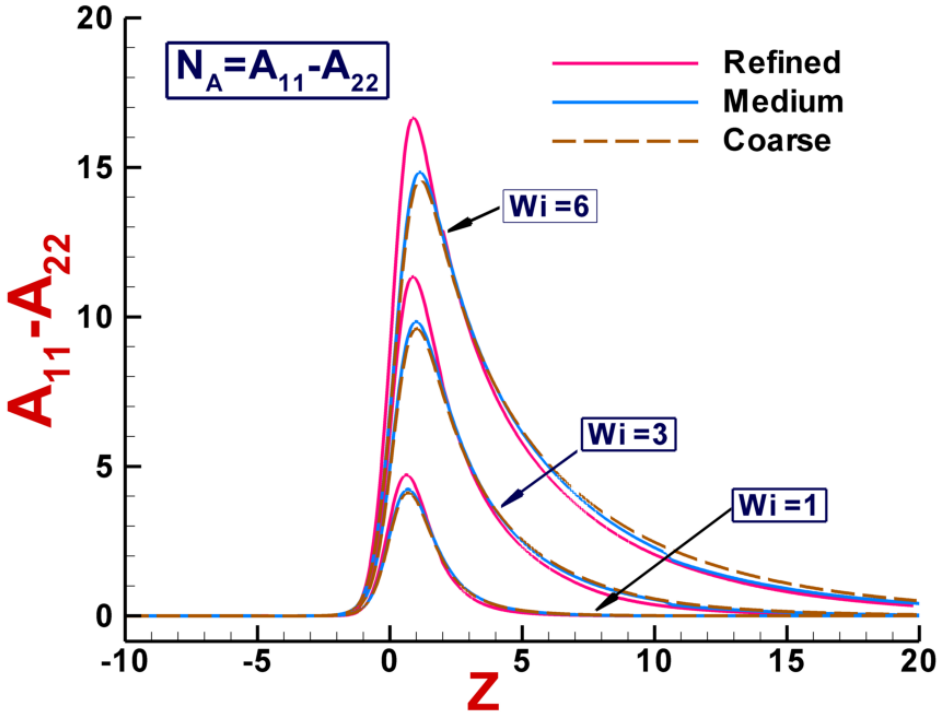

Fig 5e. (A_{11}-A_{22}) at centerline (refined, medium, coarse meshes), dissipative [sIq]-models, λ_D=0.2

Low-solvent sIq, base-geometry β_{sphere}=0.5

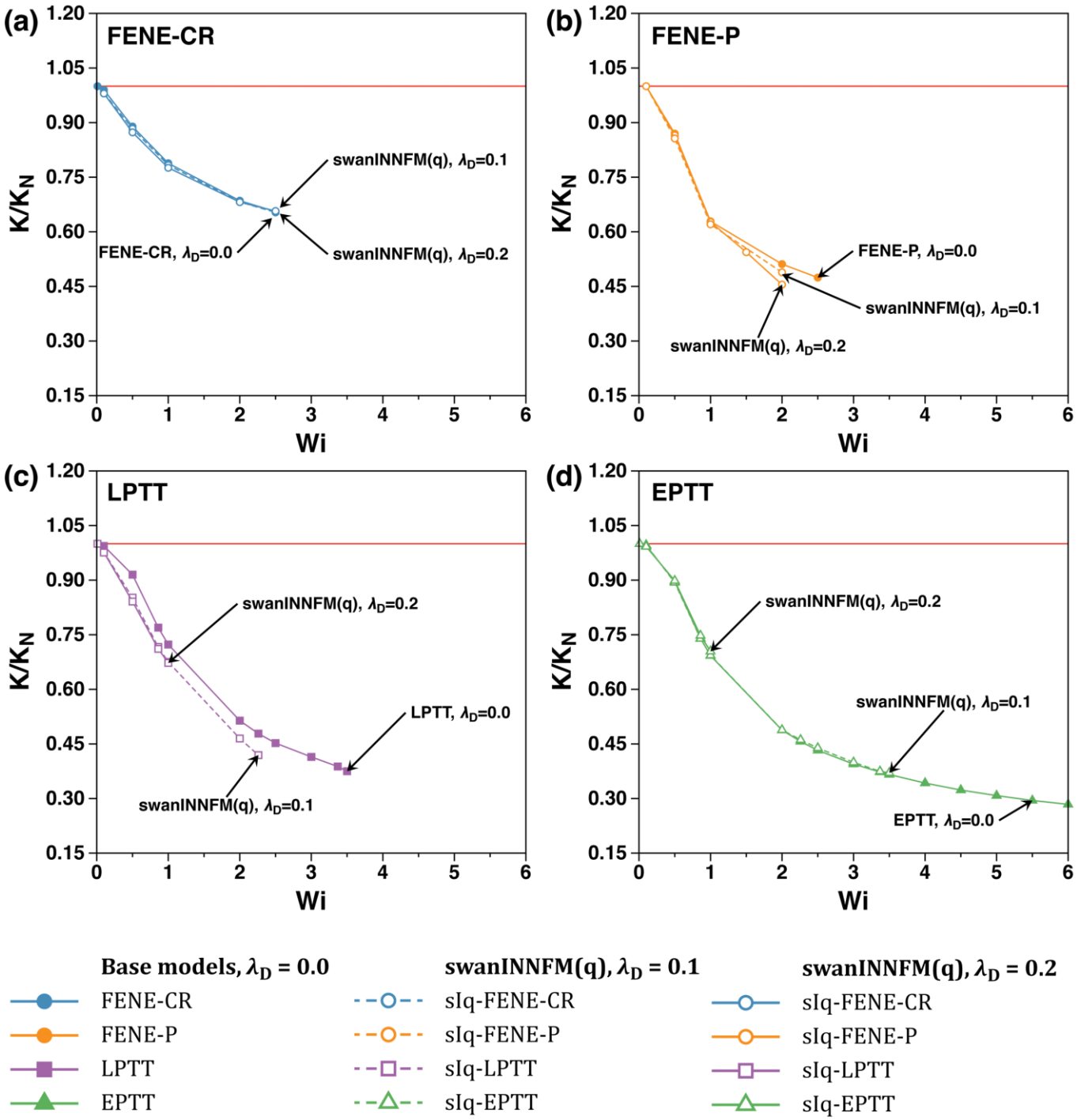

Fig 6. Drag correction factor β_{sphere}**=0.5**, $\beta_{solvent}$=1/9; dissipative [sIq]-models, 0.0≤λ_D≤0.2;

Newtonian reference

High-solvent sIq, aspect-ratio β_{sphere}=0.4

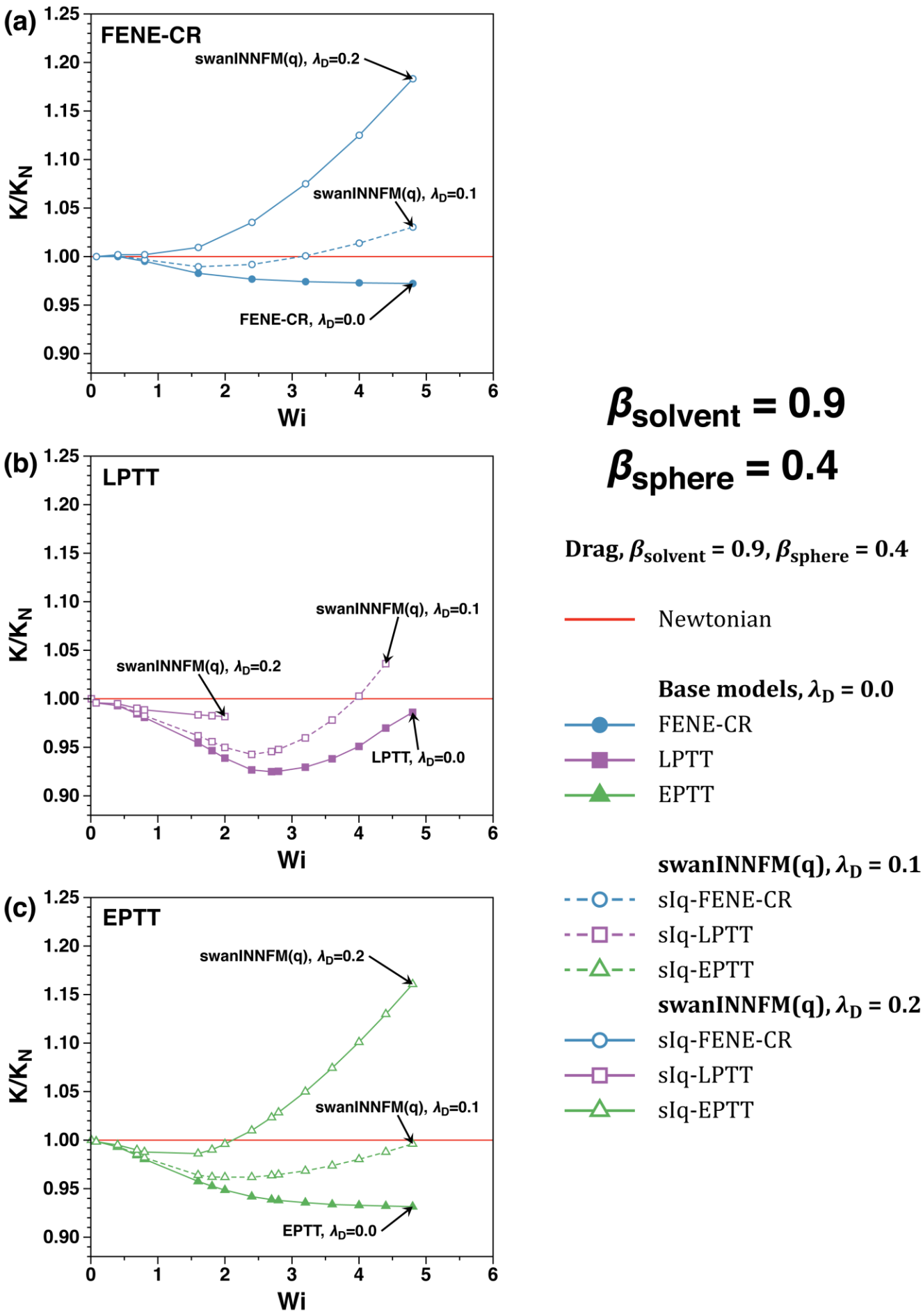

Fig 7. Drag correction factor β_{sphere}**=0.4**, $\beta_{solvent}$=0.9; dissipative [sIq]-models, $0.0 \leq \lambda_D \leq 0.2$

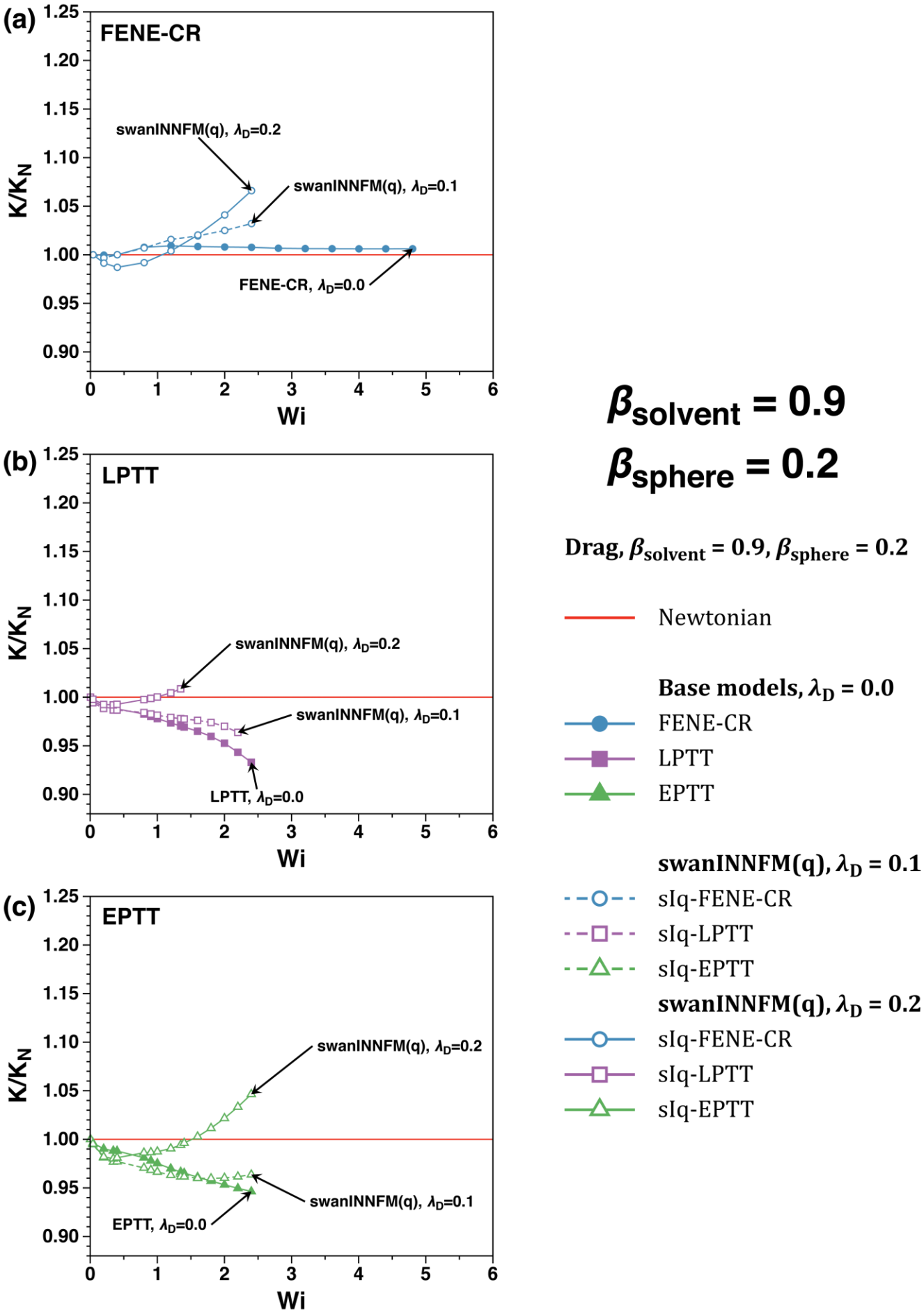

Fig 8. Drag correction factor β_{sphere}**=0.2**, $\beta_{solvent}$=0.9; dissipative [sIq]-models, $0.0 \leq \lambda_D \leq 0.2$

High-solvent sIq, comparison across geometries, fixed λ_D

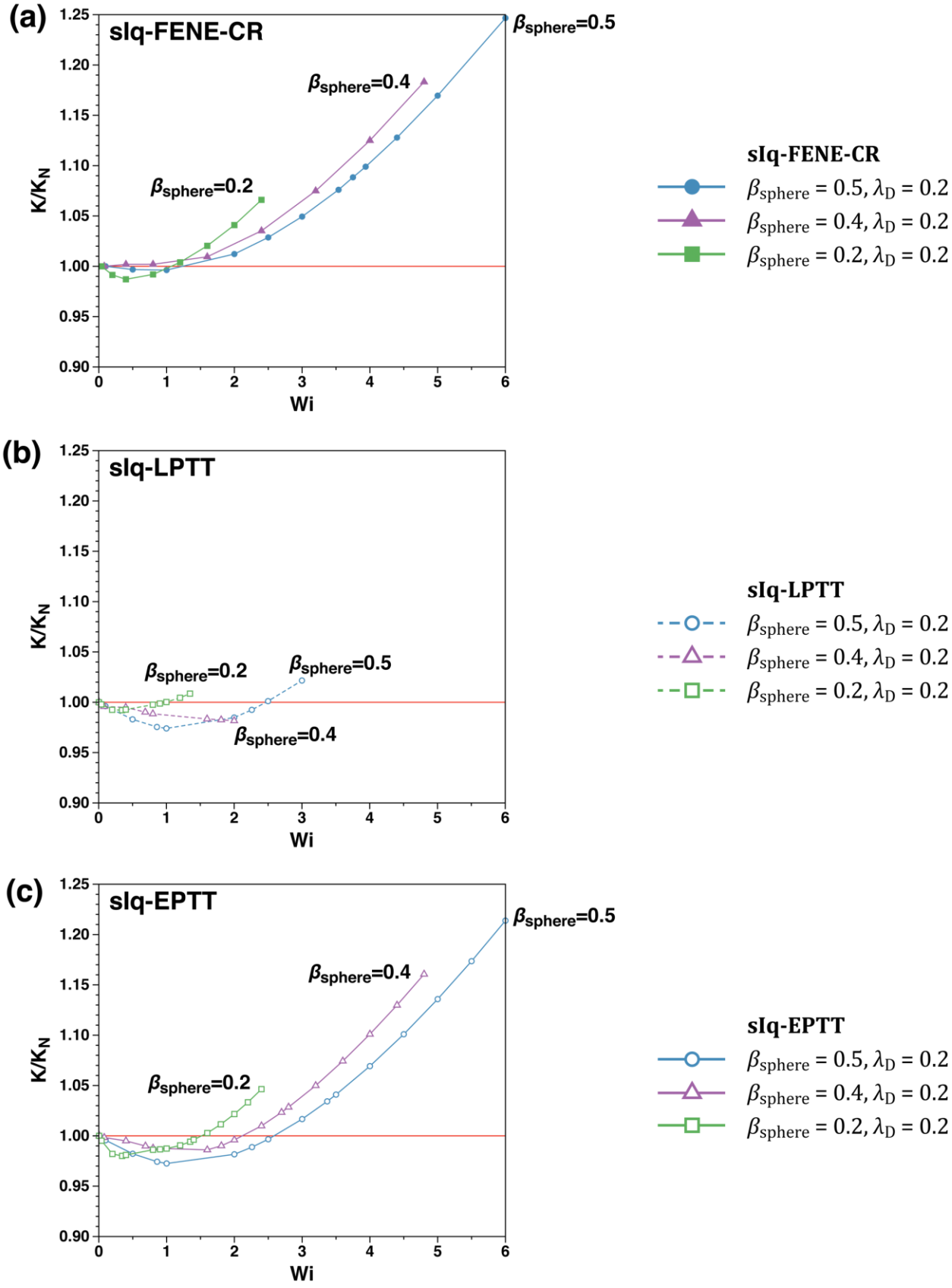

Fig 9. Drag correction factor, β_{sphere} **comparison**: dissipative [sIq]-models, $\beta_{solvent}$=0.9, λ_D**=0.2;**

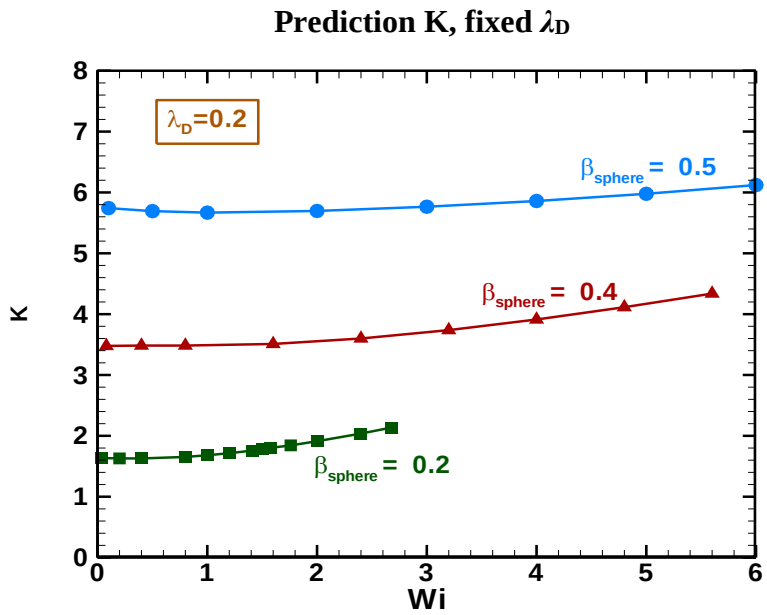

Fig 10. Drag (K) values, $\boldsymbol{\beta_{sphere}}$ **comparison**, [sIq]-FENE-CR model, λ_D=0.2; $\beta_{solvent}$=0.9